Environmental dependence in the ellipsoidal collapse model

Desjacques, V

Abstract: N-body simulations have demonstrated a correlation between the properties of haloes and their environment. In this paper, we assess whether the ellipsoidal collapse model can produce a similar dependence. First, we explore the statistical correlation that originates from Gaussian initial conditions. We derive analytic expressions for a number of joint statistics of the shear tensor and estimate the sensitivity of the local characteristics of the shear to the global geometry of the large scale environment. Next, we concentrate on the dynamical aspect of the environmental dependence using a simplified model that takes into account the interaction between a collapsing halo and its environment. We find that the tidal force exerted by the surrounding mass distribution causes haloes embedded in overdense regions to virialize earlier. An effective density threshold whose shape depends on the large scale density provides a good description of this environmental effect. We show that, using this approach, a correlation between formation redshift, large scale bias and environment density naturally arises. The strength of the effect is comparable, albeit smaller, to that seen in simulations. It is largest for low mass haloes and decreases as one goes to higher mass objects. Furthermore, haloes that formed early are substantially more clustered than those that assembled recently. On the other hand, our analytic model predicts a decrease in median formation redshift with increasing environment density, in disagreement with the trend detected in overdense regions. However, our results appear consistent with the behaviour inferred in relatively underdense regions. We argue that the ellipsoidal collapse model may apply in low density environments where nonlinear effects are negligible

DOI: https://doi.org/10.1111/j.1365-2966.2008.13420.x

Mon. Not. R. Astron. Soc. **000**, 1–23 (0000) Printed 31 January 2011 (MN LATEX style file v2.2)

Environmental dependence in the ellipsoidal collapse model

Vincent Desjacques
Racah Institute of Physics, The Hebrew University, Jerusalem 91904, Israel
E-mail: dvince@phys.huji.ac.il

ABSTRACT

N-body simulations have demonstrated a correlation between the properties of haloes and their environment. In this paper, we assess whether the ellipsoidal collapse model, whose dynamics includes the tidal shear, can produce a similar dependence. First, we explore the statistical correlation that originates from Gaussian initial conditions. We derive analytic expressions for a number of joint statistics of the shear tensor and estimate the sensitivity of the local characteristics of the shear to the global geometry of the large scale environment. Next, we concentrate on the dynamical aspect of the environmental dependence using a simplified model that takes into account the interaction between a collapsing halo and its environment. We find that the tidal force exerted by the surrounding mass distribution alters the axes collapse and causes haloes embedded in overdense regions to virialize earlier. The environment density is the key parameter in determining the virialization redshift, while the environment asphericity primarily contributes to the increase in the scatter of the critical collapse density. An effective density threshold whose shape depends on the large scale density provides a good description of this environmental effect. Such an interpretation has the advantage that the excursion set formalism can be applied to quantify the environmental dependence of halo properties. We show that, using this approach, a correlation between formation redshift, large scale bias and environment density naturally arises. The strength of the effect is comparable, albeit smaller, to that seen in simulations. It is largest for low mass haloes ($M \ll M_\star$), and decreases as one goes to higher mass objects ($M > M_\star$). Furthermore, haloes that formed early are substantially more clustered than those that assembled recently. On the other hand, our analytic model predicts a decrease in median formation redshift with increasing environment density, in disagreement with the trend detected in overdense regions. However, our results appear consistent with the behaviour inferred in relatively underdense regions. We argue that the ellipsoidal collapse model may apply in low density environments where nonlinear effects are negligible.

Key words: cosmology: theory — gravitation — dark matter — galaxies: haloes —

1 INTRODUCTION

In standard scenarios of structure formation, dark matter haloes grow hierarchically from initially small, Gaussian fluctuations. Properties of haloes can be studied in great detail using both N-body simulations and analytic models. The remarkably useful Extended Press-Schechter (EPS) theory predicts halo mass functions (Press & Schechter 1974; Bond *et al.* 1991), merging histories (Lacey & Cole 1993; Sheth & Lemson 1999b; Van den Bosch 2002; Neistein, Van den Bosch & Dekel 2006) and spatial clustering (Mo & White 1996; Mo, Jing & White 1997; Catelan *et al.* 1998; Sheth & Lemson 1999a) that are in reasonable agreement with the simulations. This analytic approach is based on the spherical collapse model (Gunn & Gott 1972). In this Lagrangian approximation, haloes are identified in the initial conditions and a single parameter, the initial density contrast, is needed to characterise their epoch of formation (Press & Schechter 1974). The collapse of a halo occurs when the linear density reaches a critical threshold. The fundamental properties of dark matter haloes are then obtained from the statistics of trajectories of the linear density field as a function of the smoothing scale (e.g. Bower 1991; Bond *et al.* 1991; Lacey & Cole 1993; Kauffmann & White 1993; Kitayama & Suto 1996). Although this spherical approximation works well until the first orbit crossing, it may not be accurate since perturbations in Gaussian density fields are inherently triaxial (Doroshkevich 1970; Bardeen *et al.* 1986; Jing & Suto 2002). Furthermore, the initial shear field rather than the density

has been shown to play a crucial role in the formation of nonlinear structures (e.g. Hoffman 1986, 1988; Peebles 1990; Dubinski 1992; Bertschinger & Jain 1994; Audit & Alimi 1996; Audit, Teyssier & Alimi 1997).

Unlike the spherical model whose dynamics depends on a single parameter only (the density), the ellipsoidal model that follows the evolution of triaxial perturbations can be used to ascertain the influence of the (external) tidal shear on the properties of collapsed regions. The gravitational collapse of homogeneous ellipsoids has been investigated by numerous authors over the past decades (e.g. Lynden-Bell 1964; Lin, Mestel & Shu 1965; Fujimoto 1968; Zeldovich 1970; Icke 1973; White & Silk 1979; Barrow & Silk 1981; Lemson 1993; Eisenstein & Loeb 1995; Hui & Bertschinger 1996). In the formulation of Bond & Myers (1996), initial conditions and external tides are chosen to recover the Zeldovich approximation in the linear regime. The dynamic of ellipsoidal collapse can be incorporated in various ways in the Press-Schechter formalism to predict the properties of haloes (Monaco 1995, 1997a, 1997b; Lee & Shandarin 1998; Chiueh & Lee 2001; Sheth & Tormen 2002). As pointed out by Sheth, Mo & Tormen (2001), the inclusion of nonsphericity in the dynamics introduces a simple dependence of the critical collapse density on the halo mass. The resulting first crossing distribution yields a better fit to the halo mass functions measured in N-body simulation (Sheth & Tormen 2002). However, other modifications to the original excursion set approach, such as the inclusion of non-radial degrees of freedom, might also improve the theoretical mass function (Audit *et al.* 1997; Del Popolo & Gambera 1998). It would thus be very desirable to identify additional distinctive predictions of the ellipsoidal collapse model beyond the mass function and bias to further test this theory.

While earlier numerical studies have not provided any conclusive evidence for a dependence of halo properties on environment (Lemson & Kauffmann 1999; Percival *et al.* 2003; Zentner *et al.* 2005), recent numerical investigations indicate that, at fixed halo mass, haloes in dense regions form at (slightly) higher redshift than in low density environments (Sheth & Tormen 2004; Harker *et al.* 2005). Using the Millennium Run (Springel *et al.* 2005), Gao, Springel & White (2005) have convincingly shown that the clustering of haloes of a fixed mass depends on formation time. This dependence is strong for haloes with mass less than the typical collapsing mass $M_\star$, and fades rapidly for $M > M_\star$. Subsequent studies have demonstrated that many other halo properties, such as spin parameter or concentration, correlate with the halo assembly history (Wechsler *et al.* 2006; Zhu *et al.* 2006; Gao & White 2007; Wetzel *et al.* 2007; Jing, Suto & Mo 2007). Also, haloes that have undergone major mergers may be more strongly clustered relative to other haloes of the same mass (e.g. Furlanetto & Kamionkowski 2006). These results call into question the simplest descriptions of structure formation based on the statistics of random walks (Bond *et al.* 1991; Lacey & Cole 1993; White 1996). However, relaxing the assumption of sphericity and/or sharp k-space filtering can introduce a dependence on environment (Zentner 2007; Sandvik *et al.* 2007). In the ellipsoidal model, the time required for a given overdensity to virialize increases monotonically with the initial shear (Sheth, Mo & Tormen 2001). Therefore, as recognised by Wang, Mo & Jing (2006), the ellipsoidal dynamics should give an environmental effect owing to the tidal field generated by the large scale environment.

In the present paper, we take an analytic approach and assess whether the ellipsoidal collapse model can produce an environmental dependence (also termed 'assembly bias') similar to that seen in N-body simulations. We start with the statistical dependence that arises in correlated (Gaussian) initial conditions. We extend the results of Doroshkevich (1970) to the joint statistics of the shear tensor. We derive conditional distributions and quantify the extent to which the asymmetry of initially triaxial perturbations is sensitive to the geometry of the large scale environment. Next, we investigate the dynamical aspect of the environmental dependence using a simplified model that takes into account the interaction between a triaxial protohalo and its environment. We find that the tidal force exerted by the surrounding mass distribution affects the axes collapse and causes haloes embedded in large overdensities to virialize earlier. A moving barrier whose shape depends on the environment density provides a good description of this environmental effect. This enables us to apply the EPS formalism in order to estimate the environmental dependence of halo properties. Our approach thus is very different than the multidimensional extension presented in Sandvik *et al.* (2007).

The paper is organised as follows. Section 2 briefly reviews the basic concepts associated with the ellipsoidal collapse model. Section §3 is devoted to the statistical correlation between the local properties of the shear and the large scale environment (Appendix B details a delicate step of the calculation). §4 investigates the dynamical origin of the environmental dependence, focusing on the distribution of halo formation redshift, large scale bias and alignment of spin parameter. Non-Markovianess and tidal interactions as potential sources of environmental dependence are discussed in §5. A final section summarises our results.

2 THEORETICAL BACKGROUND

We emphasise the role played by the shear in current theories of structure formation and introduce the basic definitions and relations relevant to the study of environmental effects in the ellipsoidal collapse model.

2.1 Shear tensor

The comoving Eulerian position of a particle can be generally expressed as a mapping $\boldsymbol{x} = \boldsymbol{q} + \mathbf{S}(\boldsymbol{q}, t)$, where $\boldsymbol{q}$ is the Lagrangian (initial) position and $\mathbf{S}$ is the displacement field. In the Zeldovich approximation (1970), the displacement field is $\mathbf{S}(q,t) = -D(t)\nabla\Phi(\boldsymbol{q})$, where $\Phi(\boldsymbol{q}) = \phi(\boldsymbol{q},t)/4\pi G\bar{\rho}_m(t)a^2D(t)$ is the perturbation potential ($\phi(\boldsymbol{q},t)$ is the Newtonian gravitational potential), $\bar{\rho}_m$ is the average matter density and $D(t)$ is the linear growth factor (Peebles 1980). The second derivatives of the perturbation potential define the deformation tensor (or strain field) $\mathrm{D}_{ij} = \partial_i\partial_j\Phi$. For convenience, we introduce the real, symmetric tensor

$$\xi_{ij}(\boldsymbol{q}) = \frac{1}{\sigma}\mathrm{D}_{ij}(\boldsymbol{q}) = \frac{1}{\sigma}\,\frac{\partial^2\Phi}{\partial q_i\partial q_j}(\boldsymbol{q})\,, \qquad (1)$$

where σ is the rms variance of density fluctuations. We will henceforth refer to ξ_{ij} as the shear tensor. Let $\lambda_1 \geq \lambda_2 \geq \lambda_3$ designate the ordered eigenvalues of ξ_{ij}. An important quantity is the probability distribution of the ordered set $(\lambda_1, \lambda_2, \lambda_3)$, first derived for Gaussian random fields by Doroshkevich (1970),

$$P(\lambda_1, \lambda_2, \lambda_3) = \frac{15^3}{8\pi\sqrt{5}}\, \Delta(\lambda)\, e^{-3s_1^2(\lambda) + \frac{15}{2} s_2(\lambda)} \;, \qquad (2)$$

where

$$\Delta(x) = \det\left(x_i^{N-j}\right) = \prod_{1 \leq i < j \leq N} (x_i - x_j) \qquad (3)$$

is the Vandermonde determinant in the arguments $x_i, i = 1, \ldots, N$, and $s_n(x)$ are the elementary symmetric functions of degree n (Weyl 1948). For three variables x_1, x_2, x_3, the first few elementary functions are

$$\begin{aligned} s_1(x) &= x_1 + x_2 + x_3 \\ s_2(x) &= x_1x_2 + x_1x_3 + x_2x_3 \\ s_3(x) &= x_1x_2x_3 \;. \end{aligned} \qquad (4)$$

If $x_1, \ldots, x_N$ are the eigenvalues of a matrix X, the functions $s_n(x)$ can be written in terms of the traces of power of X, trX^k with $k, l = 0, 1, \ldots$. For instance, $s_2(x) = (1/2)\left[(\mathrm{trX})^2 - \mathrm{tr}\left(\mathrm{X}^2\right)\right]$ etc.

2.2 Geometry of the initial density field

As shown by Bond, Kofman & Pogosyan (1996), the filamentary pattern seen in N-body simulations (e.g. Park 1990; Bertschinger & Gelb 1991; Cen & Ostriker 1993; Springel *et al.* 2005 for a recent example) is a consequence of the initial spatial coherence of the shear tensor. In this Cosmic Web paradigm, the correspondence between large scale structures in the evolved density field and local properties of the shear tensor in the initial conditions, and the knowledge of the probability $P(\lambda_1, \lambda_2, \lambda_3)$, allows us estimate the morphology of the large scale matter distribution.

The geometry of the primeval density field depends on the signature of the ordered sequence of shear eigenvalues. If, in a given region, the largest eigenvalue only is positive $(+\,-\,-)$, there is contraction along one direction and expansion in the other two so that a pancake will form. If two eigenvalues are positive while the third one is negative $(+\,+\,-)$, collapse occurs along two directions and a filament will form. The probability for these two configurations, ~ 0.84, is much larger than the probability that all three eigenvalues are positive, $P(+\,+\,+) = 0.08$. However, these values depend strongly on the density enhancement of the region under consideration. While filaments or sheet-like configurations are favoured when $\nu \lesssim 1.5$, one encounters predominantly spherical-like mass concentrations above $\nu \simeq 1.5$ (e.g. Pogosyan *et al.* 1998). Note that several methods have recently been proposed to quantify precisely the geometry and topology of density fields (e.g. Sahni *et al.* 1998; Colombi, Pogosyan & Souradeep 2000; Hanami 2001; Novikov, Colombi & Doré; Gleser *et al.* 2006).

The sequence in which these structures form is still an open problem. We briefly note that, in the pancake picture, the collapse proceeds in the order pancakes-filaments--clusters (Lin, Mestel & Shu 1965; Zeldovich 1970; Arnold, Shandarin & Zeldovich 1982). Supporting evidence comes from several N-body simulations showing first pancake-like collapse (e.g. Shandarin *et al.* 1995).

Identifying the precursors of haloes (protohaloes) in the initial conditions is another unresolved issue, despite the major advance made in the analysis of (Gaussian) random fields (Doroshkevich 1970; Adler 1981; Peacock & Heavens 1985; Bardeen *et al.* 1986; Bond & Myers 1996). Shandarin & Klypin (1984) have shown by means of simulations that massive clusters with $M \gtrsim 10^{15}\ \mathrm{M}_\odot/h$ are initially located close to local maxima of the smallest eigenvalue, with $\lambda_3 > 0$. On the other hand, recent N-body investigation (Porciani, Dekel & Hoffman 2002a,b) indicate that a large fraction of small mass haloes $M \leq M_\star$ are rather associated with primeval configurations of signature $(+\,+\,-)$. Since, at present, there is no reliable alternative to the Press-Schechter prescription, we will adopt the usual critical density criterion issued from the spherical collapse (see below). This restrictive collapse condition does not guarantee a strictly positive signature $(+\,+\,+)$. But in the ellipsoidal collapse model, the formation of a bound object can occur even if $\lambda_3 < 0$: once the shortest axis has collapsed, the nonlinear density causes the other two axes to collapse very rapidly (Bond & Myers 1996).

2.3 Ellipticity, prolateness and critical collapse density

The eigenvalues λ_i can be equivalently parametrised in terms of the shear ellipticity e and prolateness p, where

$$e = \frac{\lambda_1 - \lambda_3}{2\nu}, \quad p = \frac{\lambda_1 - 2\lambda_2 + \lambda_3}{2\nu} \;. \qquad (5)$$

and $\nu = \delta/\sigma = \lambda_1 + \lambda_2 + \lambda_3$ is the density contrast of the region under consideration. The ordering constraint implies that $e \geq 0$ if $\nu > 0$ and $e \leq 0$ if $\nu < 0$. In all case, the shear prolateness is $-e \leq p \leq e$. In this parametrisation, extreme sheet-like (oblate) structures have $p \lesssim +\, e$ while extreme filaments (prolate) have $p \gtrsim -\, e$. Doroschkevich's formula can be used to write down the distribution $g(e, p|\nu)$ of ellipticity e and prolateness p for a given density contrast ν (e.g. Bardeen *et al.* 1986),

$$g(e, p|\nu) = \frac{1125}{\sqrt{10\pi}}\, e\left(e^2 - p^2\right) \nu^5 e^{-\frac{5}{2}\nu^2\left(3e^2 + p^2\right)} \;. \qquad (6)$$

For all ν, the maximum of this distribution occurs at

$$e_m(\nu) = 1/(\sqrt{5}\nu), \quad p_m(\nu) = 0 \;. \qquad (7)$$

Notice that the most probable value e_m is comparable to the mean ellipticity $\langle e|\nu\rangle = 3/(\sqrt{10\pi}\nu) \approx 1.20 e_m$. It depends on the smoothing scale R through $\nu \propto \delta/\sigma(R)$. At fixed R, denser regions are more likely to be spherical than less dense regions while, at fixed ν, larger regions are more likely to be spherical than smaller ones.

In the excursion set formalism (Bond *et al.* 1991; Lacey & Cole 1993), the critical collapse density encodes the details of the collapse dynamics. In the spherical collapse model, the dynamics in a given cosmological background is governed by a single parameter, namely the density. A top-hat perturbation of overdensity $\nu = \delta_{\mathrm{sc}}/\sigma$ (linearly extrapolated to present epoch) collapses at redshift $z = 0$. The (linear) critical density threshold δ_{sc} depends on the cosmology. We

have $\delta_{\rm sc} = 1.673$ for the cosmological parameters considered here (Eke, Cole & Frenk 1996; Navarro, Frenk & White 1997; Lokas & Hoffman 2001). On the other hand, in the ellipsoidal collapse dynamics, the evolution of a perturbation depends on the values of e, p and ν. The critical density threshold $\delta_{\rm ec}$ is always larger than the spherical value $\delta_{\rm sc}$ and is very sensitive to the initial shear (Sheth, Mo & Tormen 2001).

3 ENVIRONMENTAL EFFECT FROM THE STATISTICS OF THE INITIAL SHEAR

The statistics of the shear tensor for Gaussian random fields has been pioneered by Doroshkevich (1970) to study the formation of large scale structures. In his seminal paper, Doroshkevich calculated the probability distribution of the shear eigenvalues and ascertained the amount of material being incorporated in a pancake. Later, Doroshkevich & Shandarin (1978) reexamined the formation of sheet-like structures and derived a distribution function for the largest eigenvalue of the shear tensor. Recently, Lee & Shandarin (1998) computed conditional probability distributions for individual shear eigenvalues to obtain an analytic approximation to the halo mass function.

Here, we derive expressions for a number of joint statistics of the shear tensor upon the assumption of Gaussianity. This enables us to quantify the importance of the statistical correlation between the asphericity of triaxial collapsing regions and the shape of their large scale environment.

3.1 Analytic considerations

We confine our calculation to the case in which the components $\xi_{ij}(\boldsymbol{x})$ and $\xi_{kl}(\boldsymbol{x}')$ are smoothed on different scales, but the joint distribution is evaluated at a single comoving position $\boldsymbol{x} = \boldsymbol{x}'$. This is most relevant to the issues considered in this paper. The central results of this Section are the joint probability distribution of shear eigenvalues, eq. (22), and the conditional probability for the shear ellipticity and prolateness, eq. (26).

3.1.1 Spectral parameter

We begin with the two-point correlation functions of the shear tensor. The general form of these correlations is given in Appendix §A. Evaluated at a single comoving position $\boldsymbol{x}$, they take the simple form

$$\langle \xi_{ij}(\boldsymbol{x})\xi_{kl}(\boldsymbol{x})\rangle = \frac{\gamma}{15}\left(\delta_{ij}\delta_{kl} + \delta_{ik}\delta_{jl} + \delta_{il}\delta_{jk}\right) , \qquad (8)$$

where ξ_{ij} and ξ_{kl} are smoothed on comoving scale R_0 and R_1 respectively. The spectral parameter

$$\gamma \equiv \frac{1}{\sigma_0\sigma_1}\int_0^\infty {\rm dln}k\, \Delta^2_\delta(k)\, \hat{W}(R_0,k)\hat{W}(R_1,k) , \qquad (9)$$

$0 \leq \gamma \leq 1$, is a measure of the correlation between these scales. Here, $\Delta^2_\delta(k) \equiv k^3P_\delta(k)/2\pi^2$ is the dimensionless, linear density power spectrum (Peebles 1980) and σ_0 and σ_1 are the rms variances of density fluctuations smoothed on scale R_0 and R_1, respectively. R_i is the comoving characteristic scale of the spherically symmetric window function $\hat{W}(R_i,k)$. Many choices are possible for this filtering function. We will adopt a top-hat filter throughout this paper. The top-hat smoothing radius R_i defines a mass scale $M_i = (4\pi/3)\bar{\rho}_m R_i^3$ so that, for a given power spectrum, σ_i, M_i and R_i are equivalent variables. Note also that, instead of writing explicitely the smoothing radius, we will use subscripts to distinguish quantities at different smoothing lengths. We will reserve the subscript 1 for haloes and the subscript 0 for the environment, assumed uncollapsed at $z = 0$.

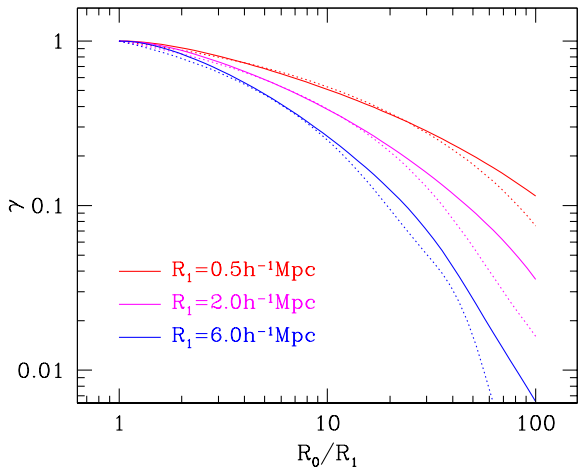

Figure 1. The spectral parameter γ as a function of the ratio R_0/R_1 for three different smoothing lengths $R_1 = 0.5$, 2 and 6 h^{-1}Mpc (solid curves from top to bottom). These values correspond to a mass scale $M_1 = 3.3\times10^{10}$, 2.2×10^{12} and 5.8×10^{13} $\mathrm{M}_\odot/h$, respectively. The dotted curves show the scaling $\gamma \propto (R_1/R_0)^{-(3+n_{\rm eff})/2}$ (see text). In all cases, γ is large even on scales $R_0 \gg R_1$.

Fig. 1 shows the correlation strength γ as a function of R_0 for three different values of R_1 : 0.5, 2 and 6 h^{-1}Mpc (curves from top to bottom). The curves have been computed for a ΛCDM model of spectral index $n_s = 0.96$ and normalisation $\sigma_8 = 0.83$ using the fitting formulae of Eisenstein & Hu (1999). This choice is consistent with the constraints inferred from the latest CMB measurements (WMAP3, see Spergel *et al.* 2006). For the special case of a power-law spectrum $P_\delta(k) \propto k^n$, the parameter γ scales with the smoothing lengths R_0 and R_1 as

$$\gamma \propto \left(\frac{R_1}{R_0}\right)^{(3+n)/2} . \qquad (10)$$

Strictly speaking, this expression is valid for a power-law spectrum only. However, it provides a reasonable approximation in the ΛCDM cosmology considered here if the spectral index n is replaced by an effective index $n_{\rm eff}(k) \equiv {\rm dln}P_\delta(k)/{\rm dln}k$ evaluated on scale $k \sim 1/R_0$. The scaling $\gamma \propto (R_1/R_0)^{-(3+n_{\rm eff})/2}$ is plotted as dotted curves in Fig. 1. Recall that the spectral index is close to $n_{\rm eff} \sim -2$ on comoving scales $1 - 10$ h^{-1}Mpc.

3.1.2 Joint statistics of the shear tensor

Owing to the symmetry of ξ_{ij}, only six components are independent. We adopt the notation of Bardeen *et al.* (1986) and label them by ξ_A, where the components $A = 1,\ldots,6$

of the six-dimensional vector refer to the components $ij = 11, 22, 33, 12, 13, 23$ of the tensor. The joint probability distribution $P(\xi_0, \xi_1)$ of the shear tensor ξ_0 and ξ_1, smoothed on scale R_0 and R_1 respectively, is given by a multivariate Gaussian whose covariance matrix M has 12 dimensions. This 12×12 matrix may be partitioned into four 6×6 block matrices, $\mathrm{M}_1 = \langle \xi_1 \xi_1^\top \rangle$ in the top left corner, $\mathrm{M}_2 = \langle \xi_0 \xi_0^\top \rangle$ in the bottom right corner, $\mathrm{B} = \langle \xi_0 \xi_1^\top \rangle$ in the bottom left corner and its transpose $\mathrm{B}^\top$ in the top right corner. Following Bardeen *et al.* (1986), we transform the six dimensions $\{\xi_{0,A}, \xi_{1,A}, A = 1, 2, 3\}$ to a new set of variables $\{u_k, v_k, w_k, k = 0, 1\}$, where

$$\begin{aligned} u_k &= \xi_{k,1} + \xi_{k,2} + \xi_{k,3} \\ v_k &= \frac{1}{2}\left(\xi_{k,1} - \xi_{k,3}\right) \\ w_k &= \frac{1}{2}\left(\xi_{k,1} - 2\,\xi_{k,2} + \xi_{k,3}\right) \ . \end{aligned} \tag{11}$$

With these definitions,

$$\begin{aligned} &\langle u_k^2 \rangle = 1, \quad \langle v_k^2 \rangle = \frac{1}{15}, \quad \langle w_k^2 \rangle = \frac{1}{5} \\ &\langle u_0 u_1 \rangle = \gamma, \quad \langle v_0 v_1 \rangle = \frac{\gamma}{15}, \quad \langle w_0 w_1 \rangle = \frac{\gamma}{5} \ , \end{aligned} \tag{12}$$

The other correlations are zero. For the six remaining components $\{\xi_{0,A}, \xi_{1,A}, A = 4, 5, 6\}$, the correlations functions are

$$\begin{aligned} \langle \xi_{0,A} \xi_{0,B} \rangle &= \langle \xi_{0,A} \xi_{0,B} \rangle = \frac{1}{15}\,\delta_{AB} \\ \langle \xi_{0,A} \xi_{1,B} \rangle &= \frac{\gamma}{15}\,\delta_{AB} \ . \end{aligned} \tag{13}$$

All the cross-correlations between u_k, v_k, w_k and $\xi_{0,A}$, $\xi_{1,A}$ vanish. The block matrices M_1, M_2 and B are diagonal in the basis introduced above,

$$\mathrm{M}_1 = \mathrm{M}_2 = \begin{pmatrix} \mathrm{C} & 0 \\ 0 & \mathrm{I}/15 \end{pmatrix}, \quad \mathrm{B} = \begin{pmatrix} \gamma\mathrm{C} & 0 \\ 0 & \gamma\mathrm{I}/15 \end{pmatrix} \ , \tag{14}$$

where $\mathrm{C} = \mathrm{diag}(1, 1/15, 1/5)$ and I is the 3×3 identity matrix. The quadratic form which appears in the joint probability distribution

$$P(\xi_0, \xi_1)\mathrm{d}\xi_0 \mathrm{d}\xi_1 = \frac{1}{(2\pi)^6\,|\mathrm{detM}|^{1/2}}\, e^{-Q(\xi_0,\xi_1)} \mathrm{d}\xi_0 \mathrm{d}\xi_1 \ , \tag{15}$$

where detM is the determinant of the covariance matrix M, can be computed easily using Schur's identities. The result may be expressed in terms of the elementary symmetric functions (4) or, equivalently, in terms of traces,

$$\begin{aligned} Q\left(\xi_0, \xi_1\right) = \frac{3}{4\left(1-\gamma^2\right)} \Big\{ &5\left[\mathrm{tr}\left(\xi_0^2\right) + \mathrm{tr}\left(\xi_1^2\right) - 2\gamma \mathrm{tr}\left(\xi_0 \xi_1\right)\right] \\ &- \left[\left(\mathrm{tr}\xi_0\right)^2 + \left(\mathrm{tr}\xi_1\right)^2 - 2\gamma\left(\mathrm{tr}\xi_0\right)\left(\mathrm{tr}\xi_1\right)\right] \Big\} \ , \end{aligned} \tag{16}$$

and the square-root of the determinant is given by $|\mathrm{detM}|^{1/2} = (20/15^6)(1-\gamma^2)^3$. The results are described by the correlation strength γ solely. The invariance under rotation $P\left(\xi_0, \xi_1\right) = P\left(\mathrm{R}\xi_0\mathrm{R}^\top, \mathrm{R}\xi_1\mathrm{R}^\top\right)$, where R is a real orthogonal symmetric 3×3 matrix, requires that P be a symmetric function of the eigenvalues, and thus a function of $\mathrm{tr}\left(\xi_0^k \xi_1^l\right)$, $k, l = 0, 1, \ldots$, regardless the statistical properties of ξ_{ij}. The expression (16) follows from our assumption of Gaussianity. Note also that no assumptions have been made so far about the coordinates.

3.1.3 Joint distribution of the eigenvalues

Lee & Shandarin (1998, see their Appendix B) have computed the joint probability distribution of the eigenvalues of the deformation tensor for a sharp k-space filter. However, they assume that both principal axis frames are aligned, which is not true in general.

To obtain the joint probability distribution of the ordered eigenvalues of the shear tensor, we choose a coordinate system such that the coordinate axes are aligned with the principal axes of ξ_0. Let α and λ be the diagonal matrices consisting of the three ordered eigenvalues $\alpha_1 \geq \alpha_2 \geq \alpha_3$ and $\lambda_1 \geq \lambda_2 \geq \lambda_3$ of the deformation tensors ξ_0 and ξ_1, respectively. The principal axis are labelled according to this ordering. With this choice of coordinate, $\xi_0 = \alpha$ and $\xi_1 = \mathrm{R}\lambda\mathrm{R}^\top$, where R is an orthogonal matrix that defines the orientation of the eigenvectors of ξ_1 relative to those of ξ_0. To preserve the orientation of the principal axis frames, we further impose the condition that the determinant of R must be $+1$. Namely, R belongs to the special orthogonal group SO(3). The properties of the trace imply that $\mathrm{tr}\,\xi_1 = \mathrm{tr}\,\lambda$ and $\mathrm{tr}\left(\xi_1^2\right) = \mathrm{tr}\left(\lambda^2\right)$. We note, however, that the term $\mathrm{tr}\left(\xi_0\xi_1\right) = \mathrm{tr}\left(\mathrm{R}\lambda\mathrm{R}^\top\alpha\right)$ depends on the rotation matrix.

The joint probability distribution $P(\alpha, \lambda)$ is obtained by integrating over the rotations that define the orientations of the orthonormal eigenvectors of ξ_0 and ξ_1. The volume measure $\mathrm{d}\xi$ for the space of real 3×3 symmetric matrices can be expressed in terms of the non-increasing sequence of eigenvalues t_i as

$$\mathrm{d}\xi = 8\pi^2\,\Delta\left(t\right)\mathrm{d}^3t\,\mathrm{dR} \ . \tag{17}$$

Here, dR is the invariant measure on the group SO(3) normalised to $\int \mathrm{dR} = 1$, $\Delta(t)$ is the Vandermonde determinant (eq. 3) and $\mathrm{d}^3t = \mathrm{d}t_1\mathrm{d}t_2\mathrm{d}t_3$. Since the quadratic form Q depends only on the relative orientation of the two orthonormal triads, we can immediately integrate over one of the SO(3) manifolds. The relevant volume is $8\pi^2/4 = 2\pi^2$. The factor 4 comes from not caring whether the rotated axis points in the positive or negative direction (see e.g Bardeen *et al.* 1986). The essential problem is the calculation of the integral over the rotations that define relative, distinct triad orientations. Appendix §B shows that the integral over the second SO(3) manifold can be cast into the form

$$\frac{1}{4}\int_{\mathrm{SO(3)}} \mathrm{dR}\,\exp\left[\beta\,\mathrm{tr}\left(\mathrm{R}\lambda\mathrm{R}^\top\alpha\right)\right] = \frac{e^{\beta\,\epsilon_+}}{4}\,W\left(\beta\epsilon_-, \epsilon_\alpha, \epsilon_\lambda\right) \tag{18}$$

where we have defined $\beta = (15/2)\gamma/(1-\gamma^2)$. The four independent variables ϵ_+, ϵ_-, ϵ_α and ϵ_λ are combinations of the six eigenvalues of α and λ (Wei & Eichinger 1990). We choose $\epsilon_+ = (1/3)\,\mathrm{tr}\alpha\,\mathrm{tr}\lambda$, $\epsilon_- = (1/3)\,\mathrm{tr}\tilde{\alpha}\,\mathrm{tr}\tilde{\lambda}$, $\epsilon_\alpha = (\alpha_1 - \alpha_2)/\mathrm{tr}\tilde{\alpha}$, $\epsilon_\lambda = (\lambda_1 - \lambda_2)/\mathrm{tr}\tilde{\lambda}$, where $\mathrm{tr}\tilde{\alpha} = \mathrm{tr}\alpha - 3\alpha_3$ and $\mathrm{tr}\tilde{\lambda} = \mathrm{tr}\lambda - 3\lambda_3$. With this parametrisation, $-\infty \leq \epsilon_+ \leq \infty$, $\epsilon_- \geq 0$ and $0 \leq \epsilon_\alpha, \epsilon_\lambda \leq 1$. The function $W(\beta\epsilon_-, \epsilon_\alpha, \epsilon_\lambda)$ can be written down as a double integral (eq. B9). We have found that a fifth-order expansion about $\beta\epsilon_- = 0$ (eq. B12) is accurate to within 2 per cent in the range $0 \leq \beta\epsilon_- \lesssim 1.5$. We use this truncated series in the computation of the group integral (18). The joint probability distribution $P(\alpha, \lambda)\mathrm{d}^3\alpha\,\mathrm{d}^3\lambda$ may now be formulated as

$$P(\alpha, \lambda)\mathrm{d}^3\alpha\,\mathrm{d}^3\lambda = \frac{15^6}{320\pi^2}\left(1-\gamma^2\right)^{-3} W(\beta\epsilon_-, \epsilon_\alpha, \epsilon_\lambda)$$

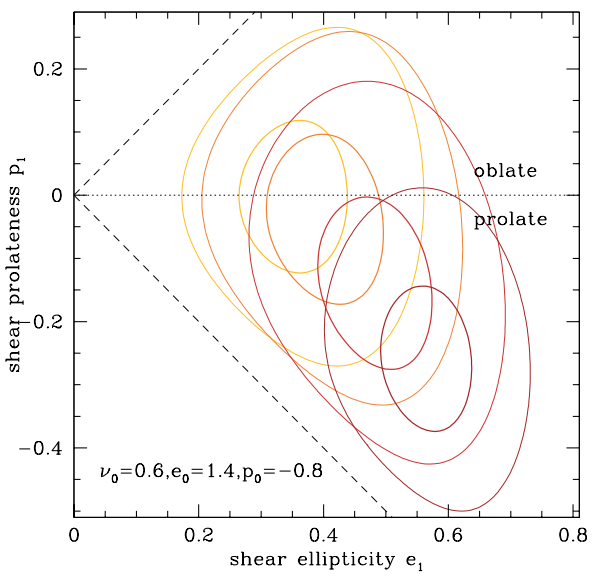

Figure 2. The 20 and 68 per cent contours of the conditional probability distribution $g(e_1, p_1|\nu_1, 0)$ for several values of the correlation strength, $\gamma = 0$, 0.4, 0.6 and 0.8 (from top to bottom). The values of (e_0, p_0, ν_0) are typical of a (prolate) filament. The dashed lines indicate the boundary of the domain $|p| \geq e$.

$$\times e^{-Q_{01}+\beta\epsilon_+}\,\Delta(\alpha)\Delta(\lambda)\,\mathrm{d}^3\alpha\,\mathrm{d}^3\lambda\,, \qquad (19)$$

where the quadratic form Q_{01} is a function of α and λ,

$$Q_{01}(\alpha,\lambda) = \frac{3}{4\left(1-\gamma^2\right)}\left\{5\left[\mathrm{tr}\left(\alpha^2\right)+\mathrm{tr}\left(\lambda^2\right)\right]\right.$$
$$\left.-\left[(\mathrm{tr}\alpha)^2+(\mathrm{tr}\lambda)^2-2\gamma\,(\mathrm{tr}\alpha)\,(\mathrm{tr}\lambda)\right]\right\}\,. \qquad (20)$$

Note that, in the limit $\gamma \ll 1$, the joint probability distribution $P(\alpha, \lambda)$ tends, as it should be, toward the product of the individual one-point probability distribution eq. (2. Using Bayes' theorem, we can easily derive the distribution of eigenvalues λ_i given the values of α_i. This conditional probability may be written as

$$P(\lambda|\alpha) = \frac{15^3}{8\pi\sqrt{5}}\left(1-\gamma^2\right)^{-3} W(\beta\epsilon_-,\epsilon_\alpha,\epsilon_\lambda)\,e^{\beta\epsilon_+}\Delta(\lambda) \qquad (21)$$
$$\times\exp\left[-\frac{15\gamma^2\mathrm{tr}\left(\alpha^2\right)+15\mathrm{tr}\left(\lambda^2\right)-3\left(\gamma\mathrm{tr}\alpha-\mathrm{tr}\lambda\right)^2}{4\left(1-\gamma^2\right)}\right]\,.$$

It can be verified by direct numerical integration that the probability distribution (22) is normalised to unity (we have used the multidimensional integrator DCUHRE described in Berntsen, Espelid & Genz 1991).

3.1.4 Joint distribution of the shear ellipticity and prolateness

The results of Section §3.1.3 can be conveniently expressed in terms of the density contrast ν, shear ellipticity e and shear prolateness p. The joint probability distribution for these variables, $g(e_1, p_1, \nu_1, e_0, p_0, \nu_0)$, is readily obtained from the following coordinate transformation,

$$\alpha_1 = \frac{\nu_0}{3}\left(1+3e_0+p_0\right) \quad \lambda_1 = \frac{\nu_1}{3}\left(1+3e_1+p_1\right)$$
$$\alpha_2 = \frac{\nu_0}{3}\left(1-2p_0\right) \qquad \lambda_2 = \frac{\nu_1}{3}\left(1-2p_1\right)$$
$$\alpha_3 = \frac{\nu_0}{3}\left(1-3e_0+p_0\right) \quad \lambda_3 = \frac{\nu_1}{3}\left(1-3e_1+p_1\right)\,. \qquad (22)$$

We have, for example, $\mathrm{tr}(\alpha) = \nu_0$, $\mathrm{d}^3\alpha = (2/3)\nu_0^2\,\mathrm{d}\nu_0\mathrm{d}e_0\mathrm{d}p_0$ and $\Delta(\alpha) = 2\nu_0^3\,e_0\left(e_0^2-p_0^2\right)$. With this parametrisation, the quadratic form Q_{01} becomes

$$Q_{01} = \frac{5}{2\left(1-\gamma^2\right)}\left[\nu_0^2\left(3e_0^2+p_0^2\right)+\nu_1^2\left(3e_1^2+p_1^2\right)+\gamma\nu_0\nu_1\right]$$
$$+\frac{1}{2}\left[\frac{\left(\nu_1-\gamma\nu_0\right)^2}{1-\gamma^2}+\nu_0^2\right]\,. \qquad (23)$$

The other variables are simply $\epsilon_+ = (1/3)\nu_0\nu_1$, $\epsilon_- = (1/3)\nu_0\nu_1\,(3e_0-p_0)\,(3e_1-p_1)$, $\epsilon_\alpha = (e_0+p_0)\,/\,(3e_0-p_0)$ and $\epsilon_\lambda = (e_1+p_1)\,/\,(3e_1-p_1)$.

Let us introduce the notational shorthands $0 \equiv (e_0, p_0, \nu_0)$ and $1 \equiv (e_1, p_1, \nu_1)$. We wish now to calculate the conditional probability $g(e_1, p_1|\nu_1, 0)$ of having an ellipticity e_1 and prolateness p_1 given a density ν_1 on scale R_1, and given the values (e_0, p_0, ν_0) on scale R_0. This probability will be useful to estimate the effect of the large scale environment on the primeval distribution of shear ellipticity and prolateness. Bayes' theorem implies that

$$g\left(e_1,p_1|\nu_1,0\right) = \frac{g\left(0,1\right)}{g\left(\nu_1,0\right)}\,. \qquad (24)$$

Since $\langle\nu_1\xi_{0,A}\rangle = \gamma/3$ if $A = 1, 2, 3$ and the other cross-correlations are zero, the calculation of the denominator is straightforward. We have $g(\nu_1, 0) = g(\nu_1|\nu_0)\,g(0)$, where

$$g(\nu_1|\nu_0) = \frac{1}{\sqrt{2\pi}}\left(1-\gamma^2\right)^{-1/2}\exp\left[-\frac{1}{2}\frac{\left(\nu_1-\gamma\nu_0\right)^2}{\left(1-\gamma^2\right)}\right]\,, \qquad (25)$$

as the density contrast ν is independent of the asymmetry parameters e and p. With these informations, the conditional probability distribution can be expressed as

$$g(e_1,p_1|\nu_1,0)\mathrm{d}e_1\mathrm{d}p_1 = \frac{1125}{\sqrt{10\pi}}\left(1-\gamma^2\right)^{-5/2}$$
$$\times\nu_1^5 e_1\left(e_1^2-p_1^2\right)W\left(\beta\epsilon_-,\epsilon_\alpha,\epsilon_\lambda\right)e^{-Q_{1|0}+\beta\epsilon_+}\mathrm{d}e_1\mathrm{d}p_1 \qquad (26)$$

where

$$Q_{1|0}-\beta\epsilon_+$$
$$= \frac{5}{2\left(1-\gamma^2\right)}\left[\gamma^2\nu_0^2\left(3e_0^2+p_0^2\right)+\nu_1^2\left(3e_1^2+p_1^2\right)\right]\,. \qquad (27)$$

As expected, in the limit where the correlation becomes weak, the conditional distribution $g(e_1, p_1|\nu_1, 0)$ reduces to the unconditional distribution, eq. (2), derived by Doroshkevich. It vanishes outside the domain defined by $|p_1| \leq e_1$. We stress that these expressions are valid for any window function. In the particular case of a sharp k-space filter however, the spectral parameter is simply $\gamma = \sigma_0/\sigma_1$.

The distribution (26) is sufficient to estimate the magnitude of the environmental effect which arises from the statistics of the initial shear field.

3.2 Statistical correlation between protohalo and environment in Gaussian initial conditions

We illustrate how the local characteristics of the shear tensor smoothed on the scale of collapsing haloes depend on the initial geometry of their large scale environment.

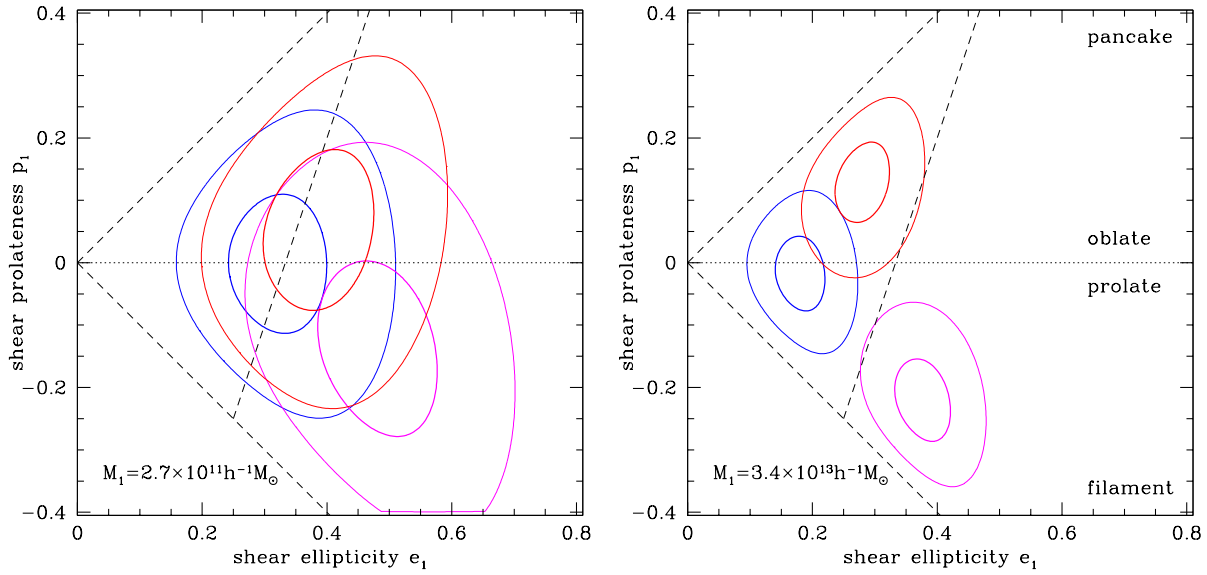

Figure 3. The 20 and 68 per cent percentiles of $g(e_1, p_1|\nu_1, 0)$ for two different halo mass $M_1 = 2.7 \times 10^{11}$ (left panel) and $M_1 = 3.4 \times 10^{13}$ $\mathrm{M}_\odot/h$ (right panel). These mass scales correspond to a smoothing radius $R_1 = 2$ and 5 h^{-1}Mpc, respectively. On large scale, the shear is smoothed on a fixed radius $R_0 = 10$ h^{-1}Mpc ($M_0 = 2.7 \times 10^{14}$ $\mathrm{M}_\odot/h$). The shape of the large scale region is either a proto-cluster, the precursor of a filament or a sheet-like structure, characterised by $(e_0, p_0, \nu_0) = (0.3, -0.1, 1)$, $(1.5, -1.3, 0.5)$ and $(1.3, 1.1, 0.4)$, respectively. The dashed lines indicate the boundary of the domain $|p_1| \geq e_1$. The interior of the triangle bounded by $(e_1, p_1) = (0, 0)$, $(\frac{1}{4}, -\frac{1}{4})$ and $(\frac{1}{2}, \frac{1}{2})$ shows the region where $\lambda_3 > 0$. For a given mass M_1, protohaloes which collapse within filament-like or sheet-like structures are, on average, initially more asymmetric than those which will form in spherical-like environment. The average asphericity and the scatter increase with decreasing halo mass.

3.2.1 Shear ellipticity and prolateness

First, it is worthwhile studying how the conditional probability distribution changes with the correlation strength γ. To this purpose, we evaluate the probability (27) for a density $\delta_1 = 2$, a value sufficiently large so that the small scale overdensity collapses at moderate to high redshift regardless of the asymmetry parameters. For a filtering scale $R_1 = 2$ h^{-1}Mpc, i.e. a halo mass $M_1 \simeq 2 \times 10^{12}$ $\mathrm{M}_\odot/h$, this corresponds to a density contrast $\nu_1 = 1.28$. On large scale $R_0 > R_1$, we take the shear ellipticity, prolateness and density to be $(e_0, p_0, \nu_0) = (1.4, -0.8, 0.6)$. These values are appropriate for a filament-like configuration. In Fig. 2, the 20 and 68 percentiles of the conditional probability distribution $g(e_1, p_1|\nu_1, 0)$ are plotted for $\gamma = 0$, 0.4, 0.6 and 0.8 (contours from top to bottom). A larger value of γ increases the asymmetry of the distribution and sharpens its maximum. Recall that, at fixed value of R_1, the correlation strength γ decreases with increasing R_0 (see Fig. 1). For instance, with $R_1 = 2$ h^{-1}Mpc and a reasonable environment size $R_0 \sim 10$ h^{-1}Mpc, we have $\gamma \sim 0.6$. The resultant distribution is displayed third from the top. In this case, the most probable values of the shear ellipticity and prolateness are $(e_m, p_m) = (0.48, -0.15)$, significantly different than those in the limit $\gamma \to 0$, namely $(0.35, 0)$. Note that the top-hat smoothing artificially reduces the asphericity of the large scale environment. Therefore, the values of e_m and p_m certainly underestimate the asymmetry that could be measured from N-body simulations (Bardeen *et al.* 1986). Finally, unless otherwise stated, we shall adopt $R_0 = 10$ h^{-1}Mpc ($M_0 = 2.7 \times 10^{14}$ $\mathrm{M}_\odot/h$) as the environment radius in the remaining of this paper.

Fig. 3 further illustrates the environmental dependence which arises from the statistical properties of the shear tensor. Contours are plotted for three different configuration shapes of the large scale environment. The halo mass is now $M_1 = 2.7{\times}10^{11}$ (left panel) and $M_1 = 3.4{\times}10^{13}$ $\mathrm{M}_\odot/h$ (right panel), and the resultant correlation coefficient is $\gamma = 0.47$ and 0.85, respectively. Also, we choose ν_1 so that $\delta_1 = 2$ in all cases. The configuration shape of the large scale region is either a proto-cluster of signature $(+\,+\,+)$, the precursor of a filament $(+\,+\,-)$, or a sheet-like structure $(+\,-\,-)$. Clearly, at fixed halo mass M_1, the protohaloes that collapse within the pancake or the filament are initially more asymmetric than those that will form in the spherical-like region. Furthermore, the asymmetry increases noticeably with decreasing halo mass. For $M_1 = 2.7 \times 10^{11}$ $\mathrm{M}_\odot/h$, the most probable values of e_1 and p_1 are $(e_m, p_m) = (0.41, 0)$, $(0.53, -0.09)$ and $(0.39, 0.06)$ respectively, whereas, for $M_1 = 3.4{\times}10^{13}$ $\mathrm{M}_\odot/h$, we find $(e_m, p_m) = (0.17, -0.02)$, $(0.37, -0.22)$ and $(0.28, 0.14)$. In the high mass halo case, the conditional distributions exhibit much less scatter as a result of the larger values of γ and ν_1.

Since the density contrast is independent of the shear ellipticity and prolateness, the probability of finding a virialized halo in a given environment of initial shape (e_0, p_0, ν_0) is modulated by $g(\nu_1|\nu_0)$, which is very sensitive to γ. For the low mass halo considered here, this probability is 0.38, 0.31 and 0.17 for the cluster, filament and pancake configurations, respectively. For the massive protohalo however, $g(\nu_1|\nu_0)$ is significantly nonzero (0.10) for the spherical-like environment solely. Thus, low mass haloes form in the mildly overdense structures of the primeval density field, while the

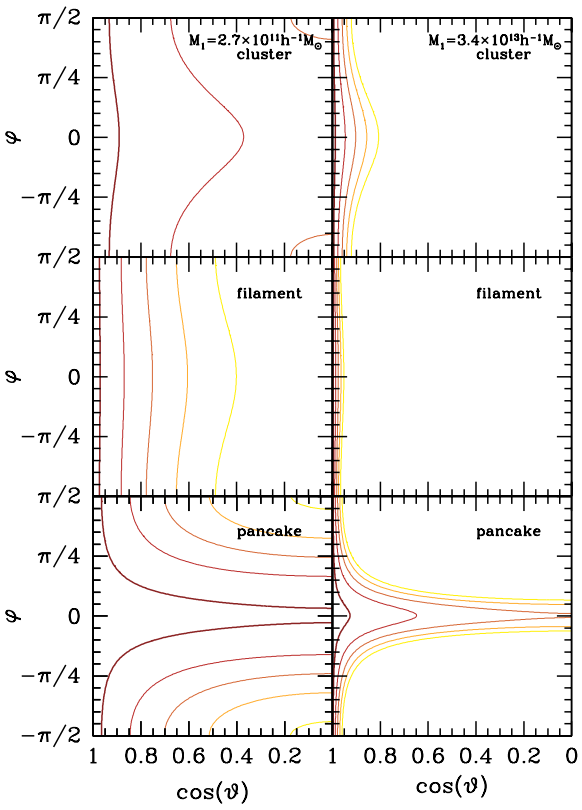

Figure 4. Contours of constant probability $P(\vartheta, \varphi|0, 1)$ for the cluster, filament and pancake-like configurations described in the text. They are shown for a halo mass $M_1 = 2.7\times10^{11}$ (left panels) and 3.4×10^{13} $\mathrm{M}_\odot/h$ (right panels). The asymmetry parameters e_1 and p_1 assume their most probable value. Levels of contours decrease by a factor of 2. ϑ is the angle between the minor axes. In all cases, the probability is highest along the vertical line $\cos\vartheta = 1$. The alignment is strongest in the case of the filament, whose minor axis coincides with the axis of symmetry.

most massive collapse mainly in the densest, weakly aspherical regions. This is a distinctive feature of hierarchical formation models (e.g. Kaiser 1984; Mo & White 1996) that adds to decrease the scatter in the relation between the environment and the local properties of the shear with increasing halo mass. This statistical effect may provide an explanation for the strong environmental dependence of low mass haloes.

3.2.2 Alignment of principal axis frames

It is fairly straightforward to derive probability distributions for the relative orientation of the principal axis frame from the results of §3.1. Appendix B provides the details of the calculation. Briefly, we parametrise the rotation matrix R in terms of the Euler angles $0 \leq \varphi, \psi \leq 2\pi$ and $0 \leq \vartheta \leq \pi$. We adopt the ZYZ convention so that ϑ is the angle between the two minor (third) axes. The trace $\mathrm{tr}\left(\mathrm{R}\lambda\mathrm{R}^\top\alpha\right)$ is then decomposed into a sum of rotation matrices $\mathcal{D}^l_{m_1,m_2}(\varphi, \vartheta, \psi)$. The integral over the variable ψ can be performed easily and yields the conditional probability $P(\vartheta, \varphi|0, 1)$ given the values of e_0, e_1 etc. In Fig. 4, contours of constant $P(\vartheta, \varphi|0, 1)$ are plotted for the cluster, filament and pancake-like configurations described above. They are shown for the halo mass $M_1 = 2.7 \times 10^{11}$ (left panels) and $M_1 = 3.4 \times 10^{13}$ $\mathrm{M}_\odot/h$ (right panels). In all cases, the asymmetry parameters e_1 and p_1 assume their most probable values. Unsurprisingly, the alignment between the minor axes of the shear smoothed on scale R_0 and R_1 is weaker for the low mass halo as a result of the smaller values of γ and ν_1. At fixed halo mass however, the alignment is substantially stronger in the case of the filamentary structure (middle panels). This mostly follows from the fact that, for a configuration shape with one or two positive eigenvalues, the alignment is strongest along the axis of symmetry, which coincides with the minor axis for a filamentary structure. Conversely, the alignment between the major axes is much stronger in the pancake configuration. These results show that the principal axis frame of the tidal tensor smoothed on the protohalo mass scale cannot be assumed independent of that defined by the environment. This is especially true when the large scale configuration shape is highly asymmetric. Accounting for this correlation has a large impact on the probability distribution of the spin parameter (see §4.4.3).

To summarise, a correlation between the local properties of the shear and the configuration shape of the environment is expected in Gaussian initial conditions because fluctuations on different scales are correlated. Our results nicely demonstrate the large magnitude of this statistical effect. At fixed halo mass, the shear of a perturbation that collapse within filaments or pancakes is on average more asymmetric than in spherical regions. The principal axis frame tends to be aligned along the axis of symmetry of the external mass distribution. Furthermore, the scatter in the relation between the primeval shear field and the geometry of the large scale environment increases strongly with decreasing halo mass. This will almost surely have a significant impact on the properties of virialized haloes in the ellipsoidal collapse model since the critical density threshold $\delta_{\rm ec}$ depends strongly on the initial values of e_1 and p_1. We will further discuss the importance of this statistical correlation in the next Section.

4 ENVIRONMENTAL DEPENDENCE IN THE ELLIPSOIDAL COLLAPSE DYNAMICS

We now concentrate on the dynamical origin of the environmental dependence in the ellipsoidal collapse model. We employ a simplified model based on the collapse of homogeneous ellipsoids that takes into account the interaction between a collapsing halo and its surroundings. To anticipate the results of this Section, we find that haloes residing in large overdensities virialize earlier. The environment density is the key parameter in determining the virialization redshift. We incorporate this dynamical effect into the excursion set formalism by means of a collapse barrier whose height depends on the environment density. This approach greatly simplifies the calculation of the environmental dependence of halo properties. It also predicts a clear correlation between formation redshift, large scale bias and environment.

4.1 Homogeneous ellipsoidal dynamics

4.1.1 Equation of motion

We consider the collapse of a triaxial perturbation embedded in a uniform background assumed to be a ΛCDM cosmology. We neglect the influence of nonlinear substructures on the gravitational evolution. The initial (Lagrangian) volume occupied by this overdense fluctuation is a (uniform) sphere of comoving radius R_1.

Following Peebles (1980) and Eisenstein & Loeb (1995), the (proper) position of any point interior to the ellipsoid is conveniently described as $r^\alpha = \mathrm{A}^{\alpha\beta} q^\beta$, where $\boldsymbol{q}^\top \boldsymbol{q} \leq 1$ and repeated indices are summed. The matrix A is a function of time solely. At all time, the equation defining the outer shell of the ellipsoid is $\boldsymbol{r}^\top \left(\mathrm{A}\mathrm{A}^\top\right)^{-1} \boldsymbol{r} = 1$. The principal axis lengths $\{A_k, k = 1, 2, 3\}$ and directions of the ellipsoid can be found by diagonalizing $\mathrm{A}\mathrm{A}^\top = \mathrm{Q}\tilde{\mathrm{A}}\mathrm{Q}^\top$, where Q is orthogonal and $\tilde{\mathrm{A}}$ is a positive definite diagonal matrix. In this model, the potential is quadratic in the coordinates, $\Phi(\boldsymbol{r}) = 1/2\, \Phi^{\alpha\beta} r^\alpha r^\beta$, so that the external and internal forces preserve the homogeneity of the protohalo at all time. Introducing the time variable $\tau = \ln(a)$ instead of t (e.g. Barrow & Silk 1981; Nusser & Colberg 1998), the equation of motion reads

$$\ddot{\mathrm{A}}^{\alpha\beta} - (1 + q(\tau))\dot{\mathrm{A}}^{\alpha\beta} = -\frac{3}{2}\Omega_m(\tau) \sum_\gamma \Phi^{\alpha\gamma} \mathrm{A}^{\gamma\beta} \,, \qquad (28)$$

and is manifestly independent of the Hubble constant. Upper dots denote derivatives with respect to τ, $q(\tau) = \Omega_m(\tau)/2 - \Omega_\Lambda(\tau)$ is the deceleration parameter ($q(\tau) = 1/2$ in a EdS Universe) and the gravitational potential Φ is in unit of $4\pi G\bar{\rho}_m$. $\Omega_m(z)$ and $\Omega_\Lambda(z)$ are the matter and vacuum density in unit of the critical density, respectively. The initial conditions are set by the Zeldovich approximation (see below). Virialization occurs when the three axes have collapsed. To prevent axis k from shrinking to arbitrary small sizes, we halt its collapse when $A_k/aR_1 = f_r \equiv 0.177$. This freeze-out radius is chosen so that the virialized object is 178 times denser than the background (Bond & Myers 1996). When axis k has collapsed, we set the radial component of the velocity and acceleration in that direction to $\dot{A}_k = \ddot{A}_k = f_r a R_1$. This way we end the radial collapse but leave the tangential velocity unchanged, so that the angular momentum of the protohalo is conserved (see, e.g., Eisenstein & Loeb 1995 for details).

4.1.2 External shear field

The external force exerted by the rest of the Universe on the triaxial perturbation may be generically written in terms of the Green function $G(\boldsymbol{r}, \boldsymbol{r}') = |\boldsymbol{r} - \boldsymbol{r}'|^{-1}$. It is natural to adopt spherical coordinates as perturbations grow from an initially homogeneous and isotropic background. The potential integral can thus be expanded as a multipole series (Binney & Tremaine 1987),

$$\Phi(\boldsymbol{r}) = \sum_{lm} (2l+1)^{-1}\, r^l\, q^>_{lm}(r)\, Y_l^m(\hat{\boldsymbol{n}}) \,, \qquad (29)$$

where $\boldsymbol{r} = r\hat{\boldsymbol{n}}$, $Y_l^m(\hat{\boldsymbol{n}})$ are the spherical harmonic functions, and the coefficients

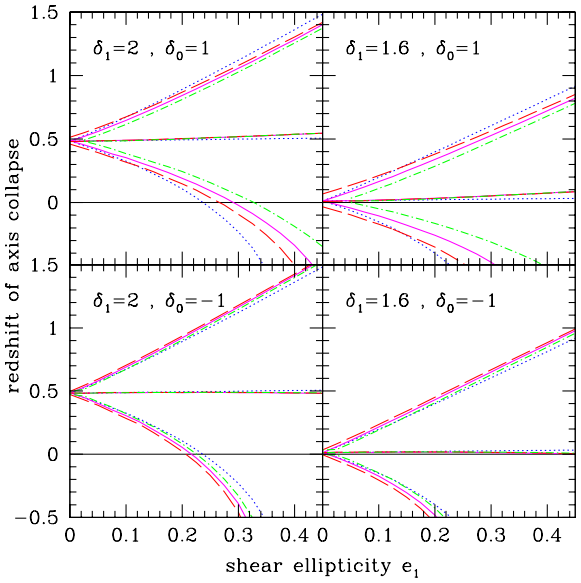

Figure 5. Collapse redshift z_c for the protohalo axes as a function of the initial ellipticity e_1. We have assumed a ΛCDM Universe. The panels show how z_c varies with the initial protohalo overdensity δ_1 and the large scale density δ_0 and shear ellipticity e_0. In all panels, $p_0 = p_1 = 0$ and the dotted curve is the reference case $(e_0, \delta_0) = (0, 0)$. The solid and dashed curves show the collapse redshifts for $(e_0, \delta_0) = (0, \pm 1)$ and $(e_0, \delta_0) = (0.3, \pm 1)$, respectively. The dotted-dashed curve also has $(e_0, \delta_0) = (0.3, \pm 1)$, but the initial alignment of the shear is weaker (see text).

$$q^>_{lm}(r) = \int \mathrm{d}^3 r'\, Y_l^m(\hat{\boldsymbol{n}}')^\dagger \delta(\boldsymbol{r}')\, (r')^{-l-1} \qquad (30)$$

are the multipole moments that characterise the potential at any (interior) point $\boldsymbol{r}$. The constant and the dipole $l = 1$ term, which corresponds to a translation, do not alter the shape of the whole region and can be dropped out. The quadrupole $l = 2$ term describes the force distorting the central region. Analytic calculation (Quinn & Binney 1992) indicate that it dominates the higher order terms ignored here. This justifies to some extent the assumption of a quadratic potential.

The quadrupole $q^>_{2m}$ of the external shear will generally not be aligned with that of the protohalo region (see §3). Although one could treat the nonlinear evolution of the external mass distribution with concentric shells (Chandrasekhar 1969; Binney & Tremaine 1987; Ryden & Gunn 1987; Eisenstein & Loeb 1995), we adopt a simpler approach and assume that the protohalo is embedded in a single, large scale triaxial region of initial comoving radius $R_0 > R_1$, not necessarily lined up with the protohalo region. In principle, the protohalo will cause the large scale perturbation to warp, producing in return a non-quadratic potential that breaks the homogeneity of the small-scale ellipsoid. To avoid this problem, we assume that the large scale triaxial perturbation and the background are unaffected by the collapse of the protohalo and remain homogeneous at all time (Icke 1973; White & Silk 1979; Eisenstein & Loeb 1995). We can therefore evolve the large scale ellipsoid independently using the model of Bond & Myers (1996).

4.1.3 Gravitational potential of the protohalo

In the principal axis frame of the large scale ellipsoid, we write down the total gravitational potential of the protohalo as

$$\Phi^{\alpha\beta} = \Phi^{\alpha\beta}_{\rm FRW} + \Phi^{\alpha\beta}_{\rm E,0} + \Phi^{\alpha\beta}_{\rm E,1} + \Phi^{\alpha\beta}_{\rm zel} \tag{31}$$

where $\Phi^{\alpha\beta}_{\rm FRW} = (1 - 2\Omega_\Lambda(\tau)/\Omega_m(\tau))/3\ \delta^{\alpha\beta}$ is the contribution of the smooth background and

$$\begin{aligned}\Phi^{\alpha\beta}_{\rm E,0} &= \frac{1}{2}\delta_0\, b_{0,\alpha}\, \delta^{\alpha\beta} \\ \Phi^{\alpha\beta}_{\rm E,1} &= \frac{1}{2}\,(\delta_1 - \delta_0)\, \sum_\gamma b_{1,\gamma}\, {\rm Q}^{\alpha\gamma}{\rm Q}^{\beta\gamma}\end{aligned} \tag{32}$$

are the gravitational potential associated with the large scale triaxial perturbation and with the remaining mass in the protohalo, respectively. The matrix elements ${\rm Q}^{\alpha\beta}(\tau)$ depend generally on τ because the protohalo may be rotating. The functions $b_\alpha(\tau)$ are defined in Appendix §C, which provides details on the potential of an homogeneous, triaxial ellipsoid. It is worth emphasising that, since $b_\alpha(\tau)$ are homogeneous of degree zero, the potentials (32) do not depend on the value of R_0 and R_1. $\delta_0(\tau)$ and $\delta_1(\tau)$ are the relative overdensity of the large scale environment and the protohalo, respectively. Since the contribution of the traceless part of both $\Phi^{\alpha\beta}_{\rm E,0}$ and $\Phi^{\alpha\beta}_{\rm E,1}$ is of second order only, we include the linear approximation for the external shear field,

$$\Phi^{\alpha\beta}_{\rm zel} = \sum_\gamma \lambda_{{\rm zel},\gamma}\, {\rm Q}^{\alpha\gamma}_i {\rm Q}^{\beta\gamma}_i\ , \tag{33}$$

where $\lambda_{{\rm zel},\gamma} = D(\tau)\,(\lambda_\gamma - \delta_1/3)$ is a linear function of the initial eigenvalues λ_γ of the shear tensor smoothed on scale R_1. ${\rm Q}^{\alpha\beta}_i = {\rm Q}^{\alpha\beta}(\tau_i)$ describes the initial orientation of the protohalo relative to that of the large scale region. This ensures that the evolution consistently reduces to the Zeldovich approximation at early times (Bond & Myers 1996). The initial conditions are explicitely

$$\begin{aligned}{\rm A}^{\alpha\beta}(\tau_i) &= a_i R_1\,(1 - D_i\lambda_\beta)\ {\rm Q}^{\alpha\beta}_i \\ \dot{\rm A}^{\alpha\beta}(\tau_i) &= {\rm A}^{\alpha\beta}(\tau_i) - a_i R_1 D_i \lambda_\beta\, {\rm Q}^{\alpha\beta}_i\ ,\end{aligned} \tag{34}$$

where $a_i = a(\tau_i)$ and $D_i = D(\tau_i)$. Note that the initial tangential velocities are zero.

The simplifications of this model notwithstanding, our calculation should provide a quantitatively useful description of the impact of environment on the collapse of dense, triaxial regions.

4.2 Effect of environment on the redshift and critical density for collapse

Our first task is to study the dynamical effect of the large scale environment on the collapse of the protohalo. Once the cosmological background is chosen, the evolution of the protohalo is governed by the initial values of (e_1, p_1, δ_1), (e_0, p_0, δ_0) and the Euler angles $(\varphi, \vartheta, \psi)$, which describe its initial orientation relative to that of the large scale ellipsoid. For simplification, we choose $p_0 = p_1 = 0$ and set $(\varphi, \vartheta, \psi) = (0.2, 0.2, 0.2)$ (in radian). Note that this particular orientation has a reasonable probability of occurring regardless of the configuration shape of the environment (see Fig. 4). The starting redshift is taken to be a hundred. We store the collapse redshift z_c of the three axes, as well as the (linear) critical density $\delta_{\rm ec}$ at virialization. Results are presented for a ΛCDM Universe with $\Omega_m = 0.238$ and $\Omega_\Lambda = 0.762$.

Fig. 5 examines how the collapse redshifts z_c of the three protohalo axes change with the model parameters. For reasons that should become apparent below, z_c is plotted against the shear ellipticity e_1. In all panels, the dotted curve is the reference case $(e_0, \delta_0) = (0, 0)$. The solid and dashed curves indicate the collapse redshifts for $(e_0, \delta_0) = (0, \pm 1)$ and $(e_0, \delta_0) = (0.3, \pm 1)$, respectively. To highlight the effect of changing the relative orientation, we have also plotted as dotted-dashed curves the collapse redshifts for $(e_0, \delta_0) = (0.3, \pm 1)$ and a weaker initial shear alignment, $(\varphi, \vartheta, \psi) = (1.5, 1.5, 1.5)$. Also shown are the values of δ_0 and δ_1, linearly extrapolated to present epoch. For positive values of δ_0, the tidal force exerted by the large scale perturbation delays the collapse along the first axis but enhances it along the third, reducing thereby the anisotropy that arises from the linear term, eq. (33). By contrast, the difference between the collapse redshift of the major and minor axis is enhanced for $\delta_0 < 0$. In all cases however, the collapse redshift of the intermediate axis is barely affected and remains close to the value predicted by the spherical collapse model. Clearly, at fixed overdensity δ_1, the haloes embedded in the large density environment virialize earlier. The strength of this effect increases with the shear ellipticity e_1. It is very sensitive to the initial conditions. For $\delta_0 = -1$, an external quadrupole shear $e_0 > 0$ delays the halo virialization as compared to the spherical case. This delay is still present for $\delta_0 = +1$ when the halo collapse is initially close to spherical (The delay is most significant for the low value of δ_1), but the trend reverses when the ellipticity gets larger than $e_1 \gtrsim 0.1$. In addition, changing the initial alignment can also increase or decrease the difference in collapse redshift. Notice also that, at low redshift, the increasing contribution of the cosmological constant to the energy density slows down the collapse of the third axis noticeably.

When all the parameters but δ_1 are held fixed, then there is a unique value of $\delta_1 = \delta_{\rm ec}(e_1, z)$ [1] which leads to the collapse of the minor axis (virialization) at redshift z. In Fig. 6, the critical density for collapse at $z = 0$ is plotted in unit of $\delta_{\rm sc}$ for the initial collapse configurations considered in Fig. 5. We have also set $p_0 = p_1 = 0$. As before, the dotted curve shows the reference case $(e_0, \delta_0) = (0, 0)$. The label 'WA' designates the configurations that have a weaker initial alignment, $(\varphi, \vartheta, \psi) = (1.5, 1.5, 1.5)$. Clearly, the critical density $\delta_{\rm ec}$ is lower for larger values of δ_0. This owes to the fact that, at fixed initial density δ_1, haloes that reside in relatively high density environments collapse earlier. Furthermore, Fig. 6 also indicates that the environment density δ_0 is the most influential parameter. The large scale ellipticity e_0, for instance, has a significant impact on the critical density $\delta_{\rm ec}$ only when $\delta_0 \gtrsim 0$. These results suggest that an average critical density $B(e_1, z, \delta_0)$ should provide a good description of this environmental effect if the scatter

[1] In what follows, we shall omit writing the other variables, but recall that $\delta_{\rm ec}$ is generally a function of the 12 variables that parametrise the shear eigenvalues and the relative orientation of the principal axis frames on scale R_0 and R_1.

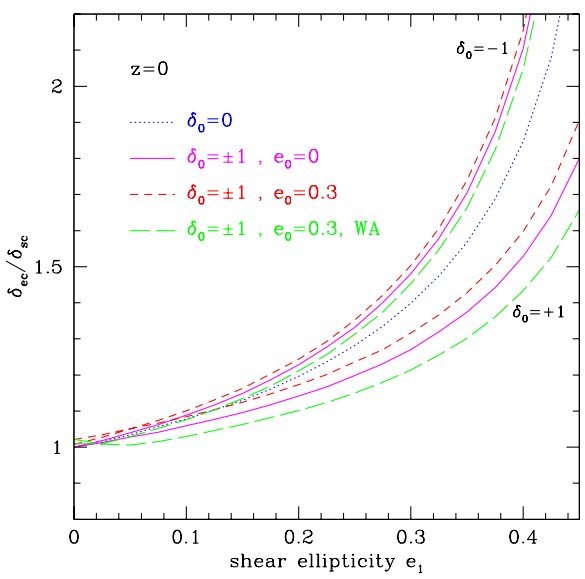

Figure 6. Critical density $\delta_{\rm ec}(e_1, z)$ for the collapse of a proto-halo perturbation at $z = 0$ in unit of $\delta_{\rm sc} = 1.673$, the critical density for a spherical collapse in the ΛCDM cosmology considered here. $\delta_{\rm ec}$ is plotted as a function of the shear ellipticity e_1. The various curves indicate how $\delta_{\rm ec}$ varies for the initial configurations considered in Fig. 5. 'WA' labels the configurations for which the initial orientation of the shear principal axis frame is given by $(\varphi, \vartheta, \psi) = (1.5, 1.5, 1.5)$ (see text). The dotted curve shows the reference case $(e_0, \delta_0) = (0, 0)$. Note that $p_0 = p_1 = 0$ in all cases.

around it is not too large. We investigate this possibility in the remainder of this Section.

4.3 Environmental dependence as moving barriers

As seen in §3, the local properties of the shear depend substantially on the large scale environment. Here, we consider a large ensemble of initial halo-environment configurations and examine the resultant distribution of critical density $\delta_{\rm ec}$. We find that it is a reasonable approximation to use an average critical density $B(e_1, z, \delta_0)$ and neglect the scatter around it. We provide a fitting formula to $B(e_1, z, \delta_0)$ which facilitates the inclusion of the environmental dependence of the kind considered here into the excursion set formalism.

4.3.1 Monte-Carlo simulations

Chiueh & Lee (2001) have shown that random realisations of the linear deformation tensor can be simulated by drawing six independent Gaussian variables. Their algorithm can be easily extended to generate joint realisations of the shear tensor which satisfy the correlation property (8). In the basis defined in eq. (11), the 12×12 covariance matrix M decomposes into a direct sum of 2×2 block-diagonal matrices. As a result, the variables $X = \{u, v, w, \xi_4, \xi_5, \xi_6\}$ can be simulated using the following linear transformation

$$X_0 = \frac{\sigma_X}{\sqrt{2}} \left(\sqrt{1+\gamma}\, y_+ - \sqrt{1-\gamma}\, y_- \right)$$

$$X_1 = \frac{\sigma_X}{\sqrt{2}} \left(\sqrt{1+\gamma}\, y_+ + \sqrt{1-\gamma}\, y_- \right) , \qquad (35)$$

where, again, the subscripts 0 and 1 indicate that the shear is smoothed on scale R_0 and R_1 respectively. y_+ and y_- are two Gaussian random deviate of dispersion unity. $\sigma_X \equiv \sqrt{\langle X^2 \rangle}$ is the rms variance in the variable X. For instance, $\sigma_X = 1/\sqrt{15}$ when $X = v$. The remaining components of the shear tensor, ξ_1, ξ_2 and ξ_3 are readily obtained from the linear relations (11).

Since the small-scale perturbation is identified as a halo at some redshift $z > 0$, while the exterior ellipsoid is assumed uncollapsed at that redshift, we constrain δ_0 so that it does not exceed $0.9\,\delta_1$. We also enforce the constraint $\delta_1 \geq 1.6$. For a radius $R_1 = 2\ h^{-1}$Mpc, this corresponds to a density threshold $\nu_1 \gtrsim 1$. In other words, the vast majority of our haloes form out of one standard deviation fluctuations. In practice, we generate random realizations of the initial conditions and reject the cases that do not satisfy these constraints.

4.3.2 Collapse barriers

We generate a large ensemble of initial collapse configurations. We evolve each realisation separately using the model described in §4.1 and store the value of the density contrast $\delta_1 \equiv \delta_{\rm ec}$ which corresponds to collapse at redshift z.

The distribution of critical density $\delta_{\rm ec}/\delta_{\rm sc}$ and shear ellipticity e_1 is plotted in Fig. 7 for several values of the primeval environment density, evenly spaced in the range $-2 \leq \delta_0 \leq 1$. Collapse occurs at $z = 0$. The crosses indicate the actual values of collapse densities and shear ellipticities of (a small subset of the) individual realisations. Also shown as the solid curve is our approximation to the critical collapse boundary $B \equiv \delta_{\rm ec}(e_1, z)$ defined by the implicit equation (Sheth, Mo & Tormen 2001)

$$\frac{\delta_{\rm ec}(e_1, z)}{\delta_{\rm sc}(z)} = 1 + \beta_1 \left[5\, e_1^2\, \frac{\delta_{\rm ec}(e_1, z)^2}{\delta_{\rm sc}(z)^2} \right]^{\beta_2} . \qquad (36)$$

The functions β_1 and β_2 generally depend on both the redshift z and the environment density δ_0. We have adopted the simple functional form

$$\beta_i(a, \delta_0) = b_i\, (1+z)^{-d_i} \exp\left(-c_i \delta_0\right) . \qquad (37)$$

The exponential factor ensures that β_1 and β_2 are strictly positive. In addition, we have enforced the constraint $d_i > 0$ to account for the (slight) decrease of the environmental dependence with redshift. Note also that, in the limit of large environment densities, the moving barrier $B(e_1, z)$ tends towards the constant spherical barrier $B = \delta_{\rm sc}(z)$. The coefficients b_i, c_i and d_i are found by fitting the barrier shape (36) to the critical collapse densities of 3×10^5 realisations with environment density in the range $-2 \leq \delta_0 \leq 1$. We find

$$b_1 \approx 0.412, \quad c_1 \approx 0.113, \quad d_1 \approx 0.0576$$
$$b_2 \approx 0.618, \quad c_2 \approx 0.0451, \quad d_2 \approx 0.0485 . \qquad (38)$$

For $\delta_0 = 0$ and $a = 1$, we obtain $\beta_1 = 0.412$ and $\beta_2 = 0.618$, in good agreement with the values inferred by Sheth, Mo & Tormen ($\beta_1 = 0.47$, $\beta_2 = 0.615$). A visual inspection of Fig. 7 has convinced us that the barrier shape (36) provides a good approximation to the increase of the critical collapse density with ellipticity and to its dependence on the environment

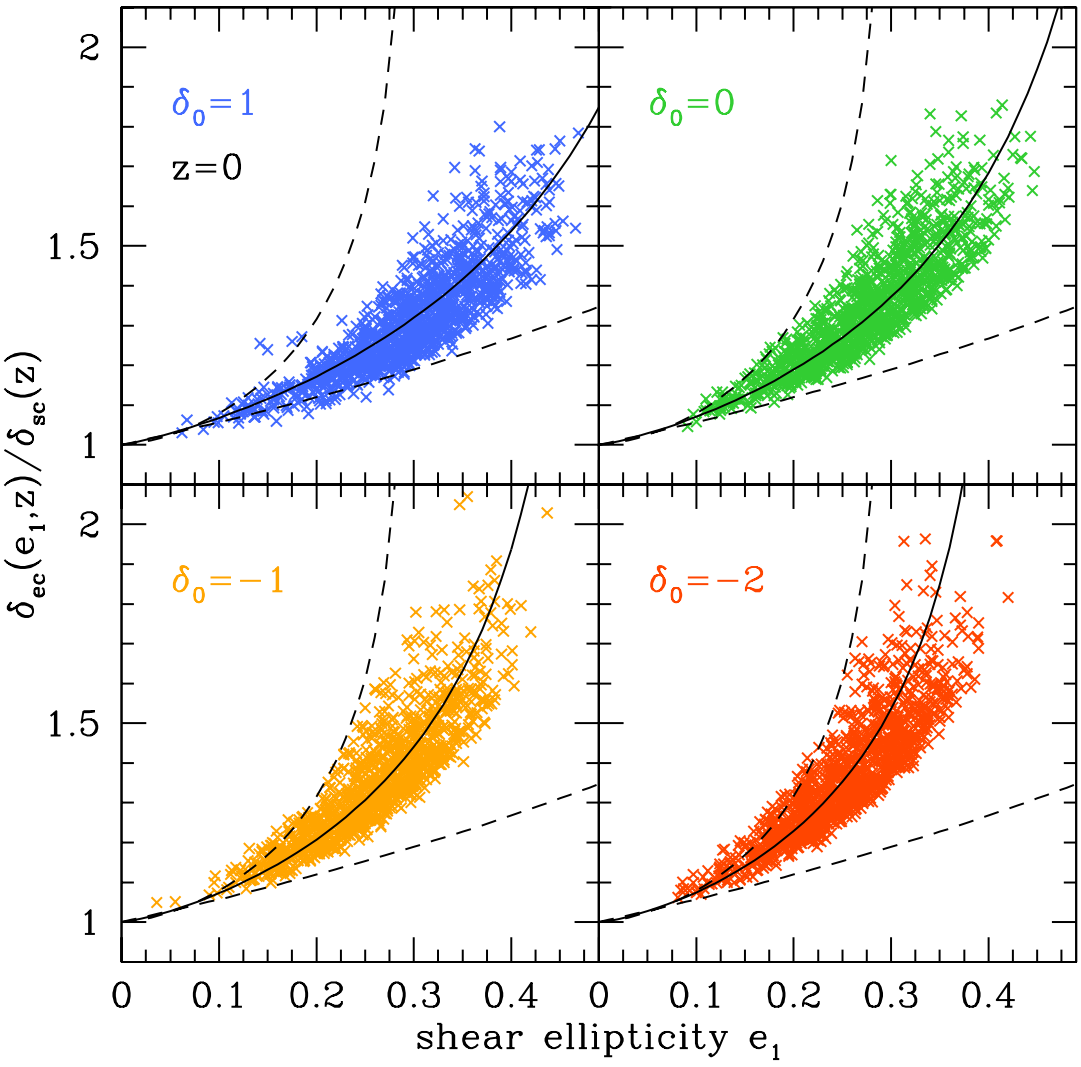

Figure 7. Distribution of critical densities $\delta_{\rm ec}$ and shear ellipticities e_1 as a function of the environment density δ_0 for a collapse redshift $z = 0$. The crosses indicate the actual values of $\delta_{\rm ec}$ and e_1 of 10^4 individual realisations. The solid curves show our approximation, eq. (36). to the critical collapse boundary. The dashed curves indicate the (approximate) boundaries of the domain $(e_1, \delta_{\rm ec})$ sampled by the random realisations. They are the barrier shape (36) with $\delta_0 = \pm 5$.

density in the range $0 \leq e_1 \leq 0.45$. To guide the eye, we have also plotted as dashed curves the (approximate) upper and lower boundaries of the domain $(e_1, \delta_{\rm ec})$ sampled by the random realisations. These boundaries are the barrier shape (36) with an environment density $\delta_0 = \pm 5$.

Following Sheth *et al.* (2001), we shall interpret (36) as a 'moving' barrier. Such an interpretation has the advantage that, once the barrier shape is known, the excursion set formalism can be use to quantify the dependence of halo properties on environment. Moreover, it is computationally more efficient that studying the first crossing distribution of multi-dimensional random walks (e.g. Chiueh & Lee 2001; Sheth & Tormen 2002; Sandvik *et al.* 2007).

4.3.3 Mass scale-ellipticity relation

Before we examine the impact of this dynamical interaction on the properties of collapsed haloes, we need to express the critical density (36) in terms of the halo mass M_1. Thus far, we have only considered the collapse of regions with initial radius $R_1 = 2\ h^{-1}$Mpc. The top panel of Fig. 8 shows the distribution of critical densities $\delta_{\rm ec}$ for three different values of R_1. The average density for collapse is plotted as the solid curve. Results are shown for an environment density $\delta_0 = 0$ only. Note, however, that we have repeated this calculation for other values of δ_0 and found good agreement between the critical densities of individual realisations and the approximation (36). This confirms that most of the environmental effect seen here arises from variation in the large scale density δ_0. At fixed R_0, changing R_1 merely affects the scatter around the collapse boundary $B(e_1, z)$, unsurprising

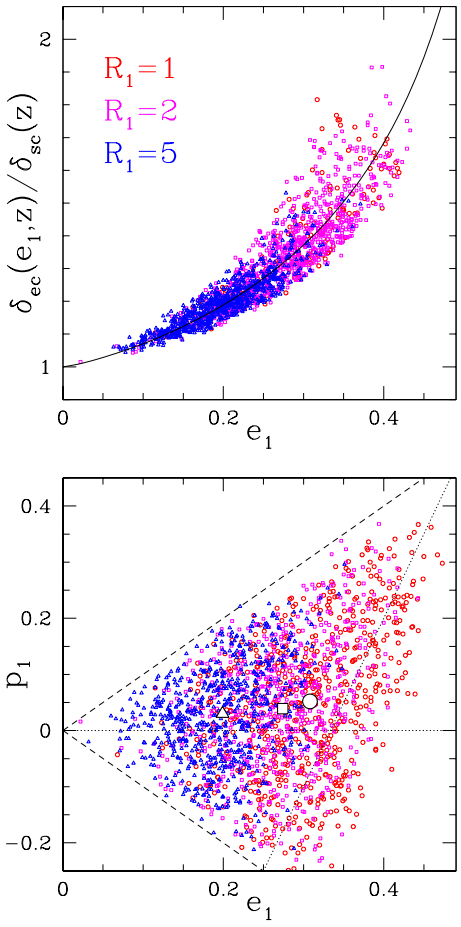

Figure 8. *Top panel* : Distribution of critical density and shear ellipticity for three different protohalo radii $R_1 = 1$ (circle), 2 (square) and 5 h^{-1}Mpc (triangle). The collapse redshift is $z = 0$ and the environment density is $\delta_0 = 0$. The average density for collapse, eq. (36), is plotted as the solid curve. *Bottom panel* : Distribution of initial shear ellipticity and prolateness for the individual realizations shown in the top panel. The interior of the triangle shows the region where $\lambda_3 > 0$. The big empty symbols indicate the peak of the distributions.

since the functions $b_i(\tau)$ that characterise the potential of the protohalo and its environment are independent of R_0 and R_1. The decrease in scatter with increasing R_1 is a direct consequence of the statistical correlation explored in §3. This is clearly seen in the bottom panel of Fig. 8, where the distribution of initial shear ellipticity and prolateness is plotted as a function of R_1. The filled symbols indicate the actual, most probable values (e_m, p_m). They increase (monotonically) with the protohalo radius R_1. This suggests relating the mass scale M_1 to the expectation value of the asymmetry parameters.

In line with the interpretation of Sheth *et al.* (2001; see also Shen *et al.* 2006; Sandvik *et al.* 2007), we use the average values (7) to translate the product $e_1\delta_1$ into a peak height $\nu(M_1, z) = \delta_{\rm sc}(z)/\sigma(M_1, z)$ [2]. Gao & White (2007) have shown that the properties of haloes in the Millennium simulation obey this scaling relation over a large redshift range. In terms of this scaled variable, the collapse boundary eq. (36) becomes

$$B(\nu, z) = \delta_{\rm sc}(z)\left[1 + \beta_1\left(\nu^2\right)^{-\beta_2}\right] . \qquad (39)$$

Sheth & Tormen (1999c) provide an analytic fit for the first crossing distribution associated to this barrier shape, which allows us to easily calculate halo properties such as formation redshift and bias.

4.4 Environmental dependence of halo properties

The main focus is to quantify the environmental dependence of halo properties arising from the moving barrier, eq. (36). Even though the ellipsoidal collapse model does not provide an excellent description of the simulations, it does nevertheless a much better job than the spherical collapse (Sheth & Tormen 1999; 2002). Therefore, the validity of a comparison between predicted and observed environmental effects should be preserved. We calculate the distribution halo of halo formation redshift and large scale bias associated to that collapse boundary. We end this Section with a discussion of the halo spin parameter.

4.4.1 Environment density and formation redshift

The halo formation redshift $z_{\rm form}$ is commonly defined as the epoch at which the main progenitor has accumulated half of its final mass. According to the EPS theory, the probability that the formation redshift of present-day haloes of mass M (we will henceforth drop the subscript 1) is larger than z is given by (Lacey & Cole 1993)

$$P(> z_f) = \int_S^{S_2} {\rm d}S' \, \frac{M}{M'(S')} f(S'|S) \, , \qquad (40)$$

where $S_2 = S(M/2)$. When the excursion set theory is combined to the ellipsoidal collapse dynamics, the conditional first crossing distribution $f(S'|S)$ shall be replaced by the following analytic formula,

$$f(S'|S) = \frac{|T(S'|S)|}{\sqrt{2\pi}(S'-S)^{3/2}} \exp\left[-\frac{\left(B(S') - B(S)\right)^2}{2(S'-S)}\right] \qquad (41)$$

where

$$T(S'|S) = \sum_{n=0}^{5} \frac{(S-S')^n}{n!} \frac{\partial^n \left[B(S') - B(S)\right]}{\partial S'^n} \, . \qquad (42)$$

This Taylor expansion provides a good fit to the conditional up-crossing probability for moving barriers of the form (39) (Sheth & Tormen 1999c). Note that the ellipsoidal collapse model predicts too many haloes with high formation redshift. The distributions are also broader than seen in the simulations (Lin, Jing & Lin 2003; Giocoli *et al.* 2007).

The differential probability distribution $P(z_{\rm form}) \equiv {\rm d}P(> z_{\rm form})/{\rm d}z_{\rm form}$ is plotted in Fig. 9 for various halo mass M and (Lagrangian) environment density δ_0. Clearly, the dependence of halo formation redshift on environment

[2] The peak height ν is the typical amplitude of fluctuations that produce haloes of mass M_1 by redshift z. A characteristic mass for clustering $M_\star(z)$ can then be defined through $\nu(M_1, z) = 1$. For the present cosmology, $M_\star(0) = 1.17 \times 10^{12}$ M$_\odot/h$.

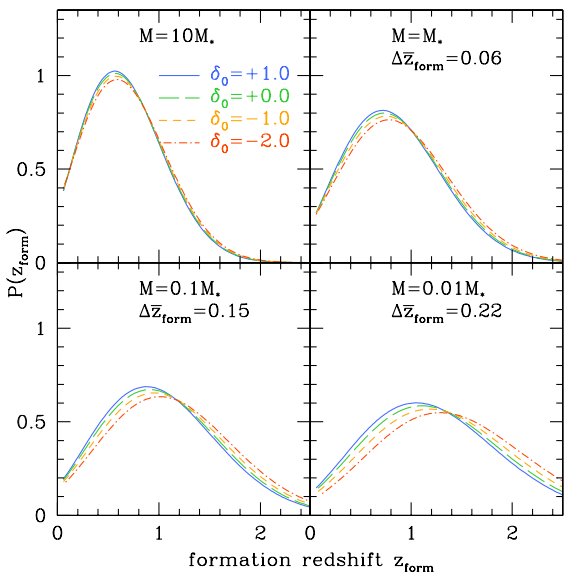

Figure 9. The differential probability distribution of formation redshift, $P(z_{\rm form})$, as a function of halo mass and (Lagrangian) environment density δ_0. $P(z_{\rm form})$ has been computed from the moving barrier (39). The halo mass is given in unit of the characteristic mass $M_\star \approx 1.2\times10^{12}\ {\rm M}_\odot/h$. For $M \leq M_\star$, we also indicate $\Delta\bar{z}_{\rm form}$, the difference between the lowest and highest median formation redshift. The mean formation redshift $\bar{z}_{\rm form}$ increases with decreasing δ_0. The effect is strongest for small mass haloes $M \ll M_\star$.

increases with decreasing halo mass. Equation (39) indeed shows that, for haloes of mass $M \gtrsim M_\star$, the critical density for collapse is $B(\nu,z) \approx \delta_{\rm sc}(z)$, weakly dependent on environment density. This is the reason why the formation redshift of massive haloes is nearly insensitive to δ_0. By contrast, random walks associated to small mass haloes $M \ll M_\star$ cross the collapse boundary $B(\nu,z)$ at relatively larger values of ν and thus induce a stronger environment effect. For $M = 0.01M_\star$, we find a median formation redshift of $\bar{z}_{\rm form} = 1.19$ for an environment density $\delta_0 = 1$. This should be compared to $\bar{z}_{\rm form} = 1.42$ when $\delta_0 = -2$. Notice that the probability distribution $P(z_{\rm form})$ is more sensitive to the exponent β_2 than the multiplicative factor β_1. The former contributes about two thirds of the environmental effect (see §5.1 for more details).

To allow for a direct comparison of our results with the analyses of N-body simulations, we need to express the environmental dependence of halo formation redshift in terms of the evolved Eulerian density. Mo & White (1996) and Sheth (1998) have shown how this may be accomplished within the spherical collapse model. The spherical collapse dynamics provides a relation between the Lagrangian radius R_0 and density δ_0 and their Eulerian counterparts R and δ. In this model, the mass interior to each perturbation is constant, giving $R_0 = R(1+\delta)^{1/3}$ if one assumes that the primeval density fluctuations are small. Furthermore, the linear density δ_0 is a monotonically increasing function of the present overdensity fluctuation δ only. Mo & White (1996) have obtained an accurate approximation to this relation for an EdS Universe,

$$\delta_0(\Delta) = \frac{\delta_{\rm sc}}{1.686}\left[1.686 - \frac{1.35}{\Delta^{2/3}} - \frac{1.124}{\Delta^{1/2}} + \frac{0.788}{\Delta^{0.587}}\right], \qquad (43)$$

where $\Delta \equiv 1+\delta$. This interpolation formula is also valid in the ΛCDM cosmology considered here provided that δ is not too large ($\delta \lesssim 10$). Ideally, we should calculate the relative numbers of patches with (R_0,δ_0) that have now evolved into regions (R,δ) (see Sheth 1998). We should also take into account the triaxiality of the large scale environment in the conversion of δ into δ_0. Henceforth however, we will neglect these complications and use the spherical approximation to relate the Lagrangian density to the Eulerian density at $z = 0$. This is sensible since, as we have seen, the linear overdensity δ_0 is the key parameter governing the correlation between collapse densities and environment. For illustration, the Lagrangian density is in the range $-3 \lesssim \delta_0 \lesssim 1$ when the Eulerian density varies between $0.3 \leq (1+\delta) \leq 5$.

Upon these assumptions, we find that the median formation redshift changes by

$$\begin{aligned} \Delta\bar{z}_{\rm form} &\approx 0.07 \quad \text{when } M = M_\star \\ \Delta\bar{z}_{\rm form} &\approx 0.33 \quad \text{when } M = 0.01M_\star\,, \end{aligned} \qquad (44)$$

when the evolved density varies in the range $-0.7 \leq \delta \leq 4$. Again, the statistical correlation induces an effect greater for low mass haloes $M \lesssim M_\star$ while, for $M \gg M_\star$, the offset in median formation redshift is barely discernible. In addition, the difference is of the magnitude seen in N-body simulations, where $\Delta\bar{z}_{\rm form} \sim 0.3-0.5$ at $M \sim 0.01M_\star$ for a large scale overdensity varying in that same range (Harker *et al.* 2006). On the other hand, our model predicts that haloes in denser regions have a lower formation redshift than those in less dense regions. This is opposite to the behaviour reported by Harker *et al.* (2006), who find that, in overdense regions, haloes in the densest environment assemble earliest. A better treatment of the relation between Lagrangian and Eulerian regions should not affect these conclusions.

Interestingly, however, these authors find that, in the most underdense regions $\delta \lesssim -0.4$, the average formation redshift increases with decreasing environment density. Despite the small number of haloes and the large scatter in formation redshift, the trend is robust, yet smaller than the effects present in the high density regions (Geraint Harker, private communication). This may be a manifestation of the environmental dependence discussed here.

4.4.2 The age-dependence of halo bias

Having established a correlation between formation redshift and environment density, we now turn to the age-dependence of the halo bias.

Mo & White (1996) and Sheth & Tormen (1999c) have shown that there is a direct relation between the halo bias and the shape of the collapse barrier. For a barrier of the form (39), the large scale bias in Eulerian space can be approximated by (Sheth *et al.* 2001)

$$b(\nu) = 1 + \frac{1}{\delta_{\rm sc}}\left[\nu^2 + \beta_1\nu^{2-2\beta_2} - \frac{\nu^{2\beta_2}}{\nu^{2\beta_2} + \beta_1\,(1-\beta_2)\,(1-\beta_2/2)}\right]. \qquad (45)$$

This bias relation is plotted in Fig. 10 as a function of the peak height ν. The dashed curve shows the halo bias at

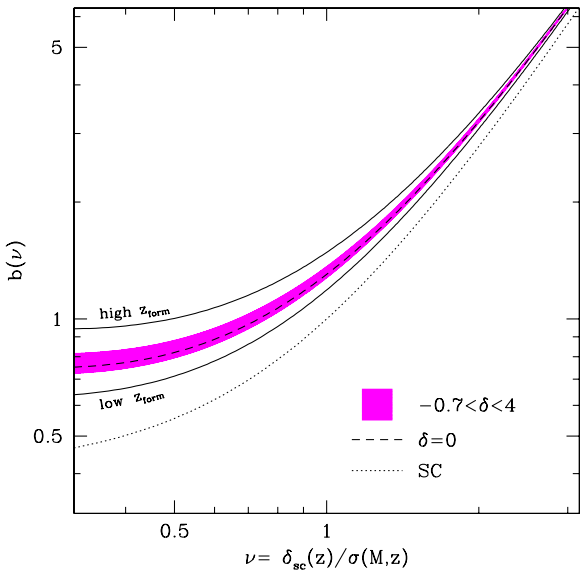

Figure 10. The large scale bias factor $b(\nu)$ as a function of the peak height $\nu = \delta_{\rm sc}/\sigma(M, z)$. The shaded area indicates the amplitude of the large scale bias when the Eulerian environment density varies in the range $-0.7 \leq \delta \leq 4$. The dashed curve is $b(\nu)$ when $\delta = 0$, whereas the dotted line indicates the prediction of the spherical collapse. The upper and lower solid curves show the bias factor of haloes which have relatively high and low formation redshifts (see text for details). Haloes that assemble relatively early are more clustered and populate the less dense regions.

mean Eulerian density $\delta = 0$, namely in the case of the ellipsoidal collapse of Sheth, Mo & Tormen (2001), while the dotted line is the prediction of the spherical collapse. The shaded area indicates the amplitude of $b(\nu)$ when the environment density varies in the range $-0.7 \leq \delta \leq 4$. The bias is roughly 10 per cent larger for the haloes residing in the most underdense region $\delta = -0.7$.

To compare our results as directly as possible with those of Gao, Springel & White (2005), it would be useful to estimate the bias factors of haloes which lie in the upper and lower tail of the formation redshift distribution. In practice, however, such a calculation proves difficult in the EPS formalism. Instead we will consider a simpler approach motivated by the relation between barrier height and median formation redshift. We have so far neglected the presence of stochasticity in critical collapse densities. In this respect, Fig. 7 shows that, at fixed environment density, there is a fairly large scatter in $\delta_{\rm ec}$. To estimate the importance of this scatter in the bias, we will also compute $b(\nu)$ for the barriers that bound the locus traced out by the random realisations when the environment density varies in the range $-0.7 \leq \delta \leq 4$ (i.e. a Lagrangian density $-2 \leq \delta_0 \leq 1$). These upper and lower barriers are shown in Fig. 7 as the dashed curves. They induce a formation redshift distribution strongly biased towards the extremes. For $M = 0.1M_\star$, the median formation redshift associated to the upper barrier is larger by $\Delta\bar{z}_{\rm form} = 0.51$ than the value obtained from the lower barrier. We use these barriers to define our 'old' (high $z_{\rm form}$) and 'young' (low $z_{\rm form}$) haloes. Of course, this is a crude approximation to the 10 (20) per cent tails considered by Gao *et al.* (2005), but we have not found any better alternative.

In Fig. 10, we show the resultant bias relations as the solid curves labelled by 'low $z_{\rm form}$' and 'high $z_{\rm form}$'. The relative bias of our old versus young haloes increases smoothly with decreasing halo mass. The effect becomes large for $\nu \lesssim 1$ because of the considerably stronger dependence of the barrier shape on the peak height. In this regime, the large scale bias of the old haloes is ∼50 per cent larger than for the young ones, an increase roughly twice as small as seen in the simulations. Overall, the behaviour is similar to that reported in Gao *et al.* (2005), where the correlation between halo clustering and formation history is strong for haloes less massive than $M_\star$ only. A better modelling of the properties of haloes lying in the tails of the formation redshift distribution is required to make a more quantitative comparison between our predictions and the measurements of Gao *et al.* (2005). The point of the present analysis is to show that the moving barrier (39) could lead to a correlation similar to that seen in N-body simulations if the scatter in collapse density is taken into account.

In contrast to the behaviour seen in N-body simulations, the predicted bias $b(\nu)$ decreases with increasing environment density, reflecting the flattening of the barrier shape for large values of δ_0. In the limit $\delta \gg 1$, $b(\nu)$ tends towards the value predicted by the spherical collapse. Since, on average, dense regions at the present time formed from relatively dense regions in the primeval fluctuation field, an anti-correlation between halo bias and large scale Eulerian density is expected in our model. This seems at first surprising but, as recognised by Abbas & Sheth (2007), the large scale bias is not necessarily a monotonically increasing function of environment density. Their results strongly suggest that haloes in extremely underdense environment are more clustered than the mean.

4.4.3 Alignment of halo spin parameter

The dimensionless spin parameter $\vec{\lambda}$ measures the amount of rigid rotation acquired by the triaxial perturbation before virialization. It is defined as (Peebles 1969)

$$\vec{\lambda} = \frac{L\sqrt{|E|}}{GM^{5/2}}\vec{\ell} \tag{46}$$

where $\vec{L} = L\vec{\ell}$ is the halo angular momentum, $\vec{\ell}$ is a unit vector, and $E = E_{\rm pot} + E_{\rm kin}$, M are the total energy and mass of the ellipsoid, respectively. The quantities L and E can be expressed in terms of the matrix elements $A^{\alpha\beta}$ (Peebles 1980; Binney & Tremaine 1987; Eisenstein & Loeb 1995). In general, the energy E of the collapsing region is not conserved, notably because the kinetic energy of the ellipsoid is altered when an axis collapses. For simplicity, we use the last value of the energy before the first axis collapses in the calculation of $\lambda = |\vec{\lambda}|$ (Eisenstein & Loeb 2005). This is a good approximation as the change in total energy is usually small during the collapse. Note also that the resulting error should be relatively small because λ depends on $\sqrt{|E|}$ solely.

The top panel of Fig. 11 illustrates the effect of including the correlation between the initial orientation of the protohalo and its large scale environment on the probability

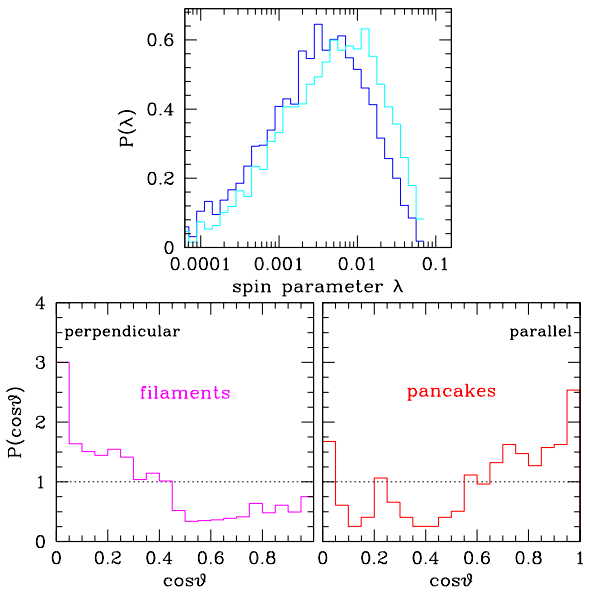

Figure 11. *Top panel* : Effect of including the correlation between the initial orientation of the protohalo and large scale environment on the probability distribution of the spin parameter λ. The left histogram shows $P(\lambda)$ when the correlations in the initial alignment are included, the right histogram when they are not. *Bottom panels* : Probability distribution of the cosine of the angle between the angular momentum of the collapsed halo and both filament direction (bottom left) and sheet normal vector (bottom right). A random distribution would be a flat line at $P(\cos\vartheta) = 1$. Results are shown for haloes that collapse at $z = 0$. The histograms were drawn from $\sim 10^4$ random realizations of the initial conditions.

distribution $P(\lambda)$ of the spin parameter. The left histogram shows $P(\lambda)$ when the correlation in the initial alignment is included, the right histogram when statistical independence is assumed. The distributions were drawn from 10^4 Monte-Carlo realizations of the initial conditions. Clearly, the inclusion of correlations in the alignment of the principal axes has a strong impact on $P(\lambda)$: It lowers the median spin by $\lesssim$40 per cent. As pointed out by several authors (Steinmetz & Bartelmann 1994; Catelan & Theuns 1996; see also Hoffman 1988), the assumption of random relative orientations overestimates the growth of angular momentum because, if the principal axis frames tend to be partially aligned, the angular momentum gain is reduced. Fig. 11 confirms that the correlation in the primeval alignment is an important factor, in agreement with the analysis of Lee & Pen (2001).

Our median spin value is $\lambda_{\rm med} \approx 0.005$, an order of magnitude lower than those found in numerical simulations, where $\lambda_{\rm med} \sim 0.03-0.05$ for haloes of mass $M \gtrsim 10^{11}\ {\rm M}_\odot/h$ (Barnes & Efstathiou 1987; Bullock *et al.* 2001; Bett *et al.* 2007). There are several reasons for this discrepancy. First, the number density of haloes of a given mass depends noticeably on the environment density δ : haloes are preferentially found in mildly overdense regions. Here, however, the distribution of evolved density δ associated to the random realisations of Fig. 11 is not representative of a fair halo sample : it peaks around $\delta = 0$, where the average spin at collapse is much lower than in high density regions $\delta \gtrsim 1$. Second, the angular momentum of a collapsing region satisfies the equation

$$\dot{L}_i = -H^{-1}\epsilon_{ijk}\,{\rm T}^{kl}\,{\rm I}^{lj}\ , \qquad (47)$$

where ${\rm T}^{ij} = (3/2)\,H^2\Omega_m(\Phi^{ij}_{\rm E,0} + \Phi^{ij}_{\rm zel})$ is the torque and ${\rm I}^{ij} = (1/5)M({\rm A}{\rm A}^\top)^{ij}$ is the inertia tensor. We note that the angular momentum vanishes to first order if the inertia tensor is zero at initial time, or if I and T are perfectly aligned (White 1984; Catelan & Theuns 1996). In this limit, the growth of angular momentum is of second order only, $L \propto a^{5/2}$, and is dominated by nonlinear effects after turnaround (Peebles 1969). This is indeed the case here as we are considering perturbations that are initially spherical. A more realistic treatment should include first-order tidal torquing. Third, our axis collapse condition strongly reduces the amount of angular momentum gained by the halo after the second axis collapses. A different prescription, such as the one adopted by Eisenstein & Loeb (1995), would increase the magnitude of the spin parameter at third axis collapse. Finally, analytic calculations indicate that a significant fraction of the angular momentum is acquired through the collapse of the outermost shells (Ryden 1988; Quinn & Binney 1992). This can only be taken into account by a detailed modelling of the matter density and velocity profiles around the collapsing haloes.

In spite of these limitations, it is worthwhile looking at the alignment between halo spin and environment as this quantity does not depend on the magnitude of the angular momentum gained during the collapse. In the bottom panels of Fig. 11, the histogram shows the alignment distribution at collapse time. The angle is measured between the angular momentum of the collapsing region and the symmetry axis/plane of the mass distribution. Clearly, haloes show a strong tendency to have their spin aligned perpendicularly to the filament or parallel to the mass sheet. This is in good agreement with the findings of Hahn *et al.* (2007; see also Sousbie *et al.* 2007) who did, however, find a clear correlation for haloes residing in sheet-like structures only. More precisely, the alignment is strongest along the second principal axis of the shear tensor. This owes to the fact that, once the first axis has collapsed, $\dot{L}_i \sim \epsilon_{ijk}\,\Phi^{kl}_{\rm E,0}\,{\rm I}^{lj}$. The growth rate is largest for the intermediate axis, $\dot{L}_2 \propto (\alpha_1 - \alpha_3)\,{\rm I}^{23}$, since the difference $\alpha_1 - \alpha_3$ [3] dominates the other two (see also Lee & Pen 2000). It is unclear whether the initial alignment between inertia and deformation tensors reported by Lee & Pen (2000) and Porciani, Dekel & Hoffman (2002b) can produce a similar correlation. We have not investigated this issue any further.

To summarise, we have demonstrated that our simplified model, which takes into account both the dynamical and statistical aspects of the ellipsoidal collapse, produces a clear correlation between formation redshift, large scale bias and environment density. The strength of the effect is of the same magnitude as seen in simulations. It is largest for low mass haloes, $M \ll M_\star$, and fades as we go to high masses, $M > M_\star$. Haloes that formed at high redshift are substantially more clustered than those that assembled recently.

[3] Here the α_is are the (ordered) eigenvalues of the large scale potential $\Phi^{ij}_{\rm E,0}$

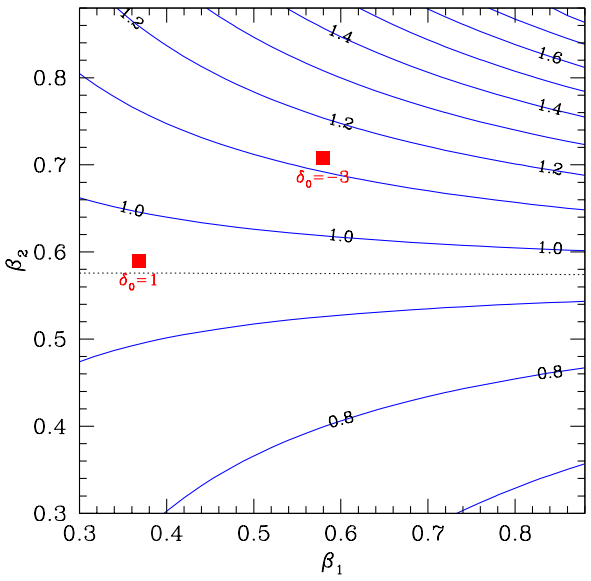

Figure 12. Sensitivity of the median formation redshift to the shape parameters β_1 and β_2. Contours of constant $\bar{z}_{\rm form}$ are plotted for a halo mass $M = 0.1M_\star$. The contour levels are evenly spaced, with an interval $\Delta\bar{z}_{\rm form} = 0.1$. The filled symbols indicate the median formation redshifts for the two extreme cases $\delta_0 = 1$ and -3 when β_1 and β_2 assume the functional form (37). The effect of varying β_1 vanishes along a critical line $\beta_2 = \beta_2^c$, where $\beta_2^c \simeq 0.58$ (dotted curve).

This is precisely the behaviour reported by Gao, Springel & White (2005). On the other hand, this model predicts a negative correlation between formation redshift and environment density, in contradiction with the trend measured by Harker *et al.* (2006). However, simulations indicate that halo properties depend on environment in a complex way : in relatively underdense regions, the average formation redshift increases with decreasing environment density (Harker *et al.* 2006) while haloes are more strongly clustered than the mean (Abbas & Sheth 2007). Our model produces an effect in the right sense. This suggests that the ellipsoidal collapse may apply in underdense regions where nonlinear effects are weak or absent.

5 DISCUSSION

In this Section, we discuss the sensitivity of the environmental effects considered above to the shape of the collapse barrier, as well as non-Markovianity and tidal interactions as potential sources of environmental dependence.

5.1 Sensitivity to the barrier shape

The strength of the environmental effect explored in §4.4 may somewhat depend on the parametrisation adopted for the moving barrier. While this is probably true for haloes of mass $M \gtrsim M_\star$, the detailed shape of the barrier should have a little impact when $M \lesssim M_\star$. In this mass range, the average collapse density $B(\nu, z)$, a Taylor series without loss of generality, should be dominated by the term of largest degree. For the simple case considered here, $B(\nu, z) \propto \beta_1 \nu^{-2\beta_2}$ when $\nu \gg 1$.

The exponent β_2 has a great influence on the correlation between formation redshift and environment density. This is clearly seen in Fig. 12, where contours of constant $\bar{z}_{\rm form}$ are plotted for a halo mass $M = 0.1M_\star$. Shown for illustration are the median formation redshifts of two extreme cases $\delta_0 = 1$ and -3 (filled symbol) when β_1 and β_2 assume the functional form (37). The parameter β_1 has a substantial impact on the formation redshift only when β_2 is far from a critical (empirically determined) value $\beta_2^c \simeq 0.58$. Along this curve, the effect of varying β_1 vanishes, presumably because the effective spectral index $n_{\rm eff}$ that controls the shape of $M(S)$ in eq. (40) conspires to maintain the median formation redshift constant. Since $n_{\rm eff}$ varies with the mass scale, we expect β_2^c to change somewhat with the halo mass. The fact that the ellipsoidal dynamics predicts a value $\beta_2 = 0.618$ close to β_2^c is a coincidence.

Regarding the environmental dependence of halo bias, note that, in the limits $\nu \gg 1$ and $\nu \ll 1$, the bias offset is $\Delta b(\nu) \approx -2\beta_1 \Delta\beta_2 \ln\nu\, \nu^{2-2\beta_2}/\delta_{\rm sc}$ to first order in $\Delta\beta_1$ and $\Delta\beta_2$. In this regime, changing the value of β_2 has a large effect on the bias of haloes lying at the extreme ends of the mass range. However, unlike the environmental dependence of formation redshift, it is the parameter β_1 that influences most the bias when the halo mass is in the range $0.1 \lesssim M/M_\star \lesssim 10$. We also note that the fitting formula (45) of Sheth, Mo & Tormen (2001) holds for β_2 strictly less than one only. It would be prudent to check again their approximation, namely, derive the first crossing distribution from a large ensemble of random trajectories when the values of β_1, β_2 differ significantly from those at mean density ($\delta_0 = 0$).

We have shown that each of the shape parameters β_1 and β_2 has a distinct impact on the halo formation redshift and large scale bias. Therefore, an environmental dependence of formation redshift and bias will be present regardless the exact values of these variables.

5.2 Environmental effect from non-Markovianity

In the excursion set formalism, a spherical symmetric window function $\hat{W}(R, k)$ is used to define the trajectories of the linear density field $\delta(R)$ as a function of smoothing scale. When the sharp k-space filter is adopted, $\delta(R)$ executes a random walk. The property of Markovianity has been exploited extensively to obtain analytic expressions for the first crossing distribution etc. This is the reason why we have considered that particular window function in the computation of halo formation redshift and bias. However, the Markov nature of Brownian walks prevents any correlation between large scale environment and assembly history (see White 1996 for a discussion). Halo merger trees are indeed non-Markovian across short time steps (Neistein & Dekel 2007). A natural way to introduce correlations would be to use another window function. This possibility has been considered by Zentner (2007; see also Peacock & Heavens 1990; Bond *et al.* 1991; Schücker *et al.* 2001; Nagashima 2001; Amosov & Schücker 2004). Here we argue that non-Markovianess should lead to an effect that is larger for high mass haloes.

For concreteness, let us consider the collapse of a perturbation of comoving size R_1. To investigate the impact of

environment on its formation history, we restrict ourselves to trajectories that obey the following two constraints :

$$C_0 : \ \delta(R_0) = \nu_0\,\sigma_0$$
$$C_1 : \ \delta(R_1) = \nu_1\,\sigma_1 \ , \qquad (48)$$

where, again, $\sigma_i = \sigma(R_i)$ and $R_0 = 10\ h^{-1}$Mpc is the scale of the large scale environment. We neglect triaxiality and choose $\nu_1 = \delta_{\rm sc}/\sigma_1$ to ensure that the halo has just collapsed by redshift $z = 0$. ν_0 can be positive or negative, depending on whether the halo forms in a high or low density region.

We can calculate the most probable trajectory $\bar{\delta}(R)$ given the constraints $\{C_i\}$. Since these are linear functional of the density field, the probability of possible realization $\delta(R)$ can be expressed as a shifted Gaussian around an ensemble mean field (see Adler 1981; Hoffman & Ribak 1991; Van de Weygaert & Bertschinger 1996 for a rigorous treatment)

$$\bar{\delta}(R) = \zeta_i(R)\,\zeta_{ij}^{-1} c_j \ , \qquad (49)$$

where $\zeta_i(R) = \langle \delta(R)\, C_i \rangle$ is the cross-correlation between the field and the ith constraint, and $\zeta_{ij} = \langle C_i C_j \rangle$ is the constraints' correlation matrix. The residual field $\tilde{\delta} = \delta - \bar{\delta}$ is a Gaussian random field which is not homogeneous nor isotropic, but whose statistical properties are independent of the $\{C_i\}$ (Hoffman & Ribak 1991). We define a normalised cross-correlation between the constraints and the field,

$$\zeta_i(R) \equiv \frac{1}{\sigma_i \sigma} \int_0^\infty {\rm dln}k\, \Delta^2_\delta(k) \hat{W}(R_i,k) \hat{W}(R,k) \ , \qquad (50)$$

where $\sigma \equiv \sigma(R)$ and $\hat{W}(R,k)$ is the tophat filter. The calculation of the matrix elements ζ_{ij} is immediate. The mean field $\bar{\delta}$ can be expressed as

$$\bar{\delta}(R) = \frac{\nu_0\,\sigma}{(1-\gamma^2)} \left\{ \zeta_1 \left(\frac{\nu_1}{\nu_0} - \gamma \right) + \zeta_0 \left(1 - \gamma\,\frac{\nu_1}{\nu_0} \right) \right\} \ . \qquad (51)$$

The variance of the residual is $\tilde{\sigma}^2(R) = \sigma^2 - \zeta_i\,\zeta_{ij}^{-1}\zeta_j$ and does not depend on the constraints C_0 and C_1. For a given mass scale $M_1 \propto R_1^3$, the difference $\bar{\delta}_+ - \bar{\delta}_-$ between the mean field of two different large scale environments with density contrast ν_+ and $\nu_- < \nu_+$ is

$$\bar{\delta}_+(R) - \bar{\delta}_-(R) = (\nu_+ - \nu_-)\ \sigma\ \frac{(\zeta_0 - \gamma\,\zeta_1)}{(1-\gamma^2)} \ . \qquad (52)$$

This difference is negative (positive) when the smoothing radius is $R < R_1$ ($R > R_1$). In other words, the density profile around $\delta(R_1)$ is steeper in low density regions. Note that, for a sharp k-space filter, $\bar{\delta}_+ - \bar{\delta}_-$ vanishes when $R < R_1$ since $\zeta_1 = \zeta_0/\gamma$, but is generally non-zero in the range $R > R_1$.

Fig. 13 shows the mean field $\bar{\delta}(R)$ for the tophat filter. $\bar{\delta}(R)$ is plotted as a function of the smoothing radius for two different halo mass $M_1 = 2.7 \times 10^{11}$ and 3.4×10^{13} $\mathrm{M}_\odot/h$. On larger scale $R_0 = 10\ h^{-1}$Mpc, the density contrast is set to $\nu_+ = 1$ (dashed curves) and $\nu_- = -1$ (solid curves). To ensure that the trajectories $\delta(R)$ describe the formation history of $M = M_1$ haloes, we should also have constrained the density so that $\delta(R)$ does not cross the barrier $\delta = \delta_{\rm sc}$ on scale larger than R_1. Here we ignore this constraint since its implementation is not straightforward when the window function differs from a sharp k-space filter. This is the reason why a substantial fraction of the trajectories penetrate

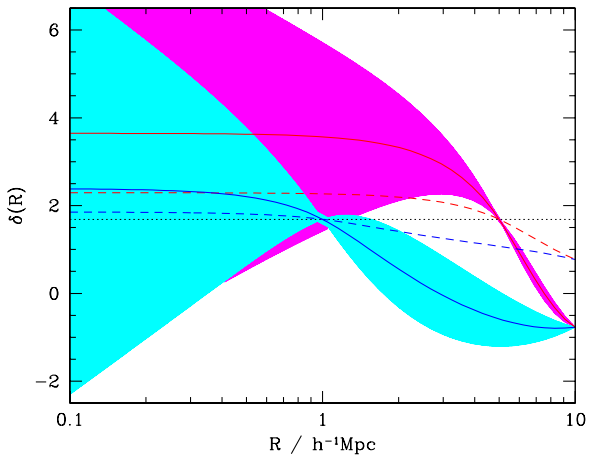

Figure 13. Mean field $\bar{\delta}(R)$ as a function of the smoothing radius R for two different halo size $R_1 = 1$ and 5 h^{-1}Mpc. The mean field obeys the following two constraints : i) $\delta(R_1) = \delta_{\rm sc}$ ii) $\delta(R_0) = \pm\sigma_0$. The solid and dashed curves show the average trajectories which satisfy $\delta(R_0) = -\sigma_0$ and $\delta(R_0) = +\sigma_0$, respectively. The shaded areas indicate the 68% scatter around the mean. For clarity, they are attached to the curves with $\delta(R_0) = -\sigma_0$ only. The horizontal line is the constant spherical collapse barrier $\delta = \delta_{\rm sc}$. Results are shown for the tophat filter.

the barrier $\delta = \delta_{\rm sc}$ on scale $R > R_1$. This caveat notwithstanding, the present calculation is adequate to understand, at least qualitatively, the effect of non-Markovianity. Notice that the difference $\bar{\delta}_+ - \bar{\delta}_-$ is approximately constant throughout most of the halo formation history ($R/R_1 \leq 1$). Most importantly, the effect is about twice as large for the high mass halo while, at fixed R/R_1, the scatter of the residual field is lower by ~ 60 per cent.

This suggests that the environmental dependence which arises from non-Markovianess is stronger for high mass haloes. This has also been pointed out by Zentner (2007). Therefore, it is unlikely to explain the trend seen in overdense regions where, undoubtedly, correlations are stronger for low mass haloes (e.g. Gao & White 2007). However, it may apply for isolated haloes in voids or underdense regions. It should also leave a signature distinct from the ellipsoidal collapse which, as we have seen, induces a stronger dependence for low mass haloes.

5.3 On tidal interactions

Irregularities in the mass distribution induce non-radial motions that slow down the collapse (Peebles & Growth 1976; Davis & Peebles 1977; Peebles 1990). This "previrialisation" conjecture is supported by the numerical investigations of, e.g., Barrow & Silk (1981); Szalay & Silk (1983); Villumsen & Davis (1986); Lokas *et al.* (1996); and by the analytic calculations of Del Popolo *et al.* (1998; 2001), which indicate that tidal heating can counterbalance the effect of the shear and delay the collapse. Recently, Wang *et al.* (2006) and Diemand *et al.* (2007) have proposed that the assembly bias seen in N-body simulations originates from tidal interactions with a larger neighbour. They have shown that, at

late time, the tidal field of massive neighbouring haloes halts the growth of haloes and, in many cases, even reduces their mass. Furthermore, tidal effects appears to have a larger influence on small mass haloes. Therefore, this could also explain why the age-dependence of clustering is stronger for low mass haloes. The large effect measured by Diemand *et al.* (2007) indicates that, in high density regions, tidal interactions are likely to overwhelm the environmental dependence arising from anisotropic collapse, and increase the average formation redshift in overdense regions.

Although the impact of tidal stripping can only be rigorously quantified with numerical simulations, the suppression of mass accretion through tidal heating could also be addressed analytically. The spherical collapse model, in which the collapsing object is divided into a series of concentric shells, seems better suited than the ellipsoidal collapse. A thorough discussion of tidal heating is beyond the scope of the present paper. Note, however, that the torque imparted by the (external) mass distribution on a thin spherical shell is $\tau(\boldsymbol{x}) \propto \int \mathrm{d}\Omega\, \tilde{\delta}(\boldsymbol{x}) \wedge \nabla\phi(\boldsymbol{x})$ (e.g. Ryden & Gunn 1987), where $\tilde{\delta}(\boldsymbol{x}) = \delta(\boldsymbol{x}) - \bar{\delta}(x)$ is the deviation from the spherically symmetric distribution $\bar{\delta}(x)$. This is $\tilde{\delta}$ which pulls the infalling matter out of its purely radial motion. In the linear regime, $\tilde{\delta}$ is a Gaussian density field statistically independent of the spherical average $\bar{\delta}(x)$. Hence, tidal heating does not induce any environmental dependence at first order. Consequently, modelling the growth of nonlinearities in the surrounding mass distribution will be crucial to ascertain analytically the importance of tidal heating in the environmental dependence of halo collapse.

6 CONCLUSION

The ellipsoidal collapse model is an extension of the spherical dynamics that takes into account the anisotropic collapse of triaxial perturbations. This non-spherical dynamics provides a substantially better description of halo statistics such as mass function and large scale bias. It is, however, unclear whether the ellipsoidal collapse can induce environmental effects similar to that seen in N-body simulations.

In this paper, we have attempted to address this issue, paying special attention to both the statistical and dynamical origin of the environmental dependence. In a first part, we have explored the statistical correlation that arises in (Gaussian) initial conditions between the local properties of the shear and the configuration of the large scale environment. To this purpose, a number of joint statistics for the shear tensor have been derived, thereby extending the previous analysis of Doroshkevich (1970). In a second part, we have examined the dynamical aspect of the environmental dependence using a simplified model that takes into account the interaction between a collapsing, ellipsoidal perturbation and its large scale environment. Relaxing the assumption of sphericity (at the heart of the spherical collapse) introduces a dependence of collapse redshift on environment. The tidal force exerted by the surrounding mass distribution alters the collapse of the major and minor axes, and causes haloes embedded in large overdensities to virialize earliest. We have found that the environment density is a key parameter in determining the virialization redshift, the large scale asphericity contributing mostly to increase the scatter in collapse density. An effective barrier whose shape depends on the large scale density provides a good description of this environmental effect. Such an interpretation has the advantage that the EPS formalism can be applied to estimate the environmental dependence of halo properties like formation redshift and large scale bias.

We have shown that, using this moving barrier approach, a correlation between formation redshift, large scale bias and environment density naturally arises. The magnitude of the effect is similar, albeit smaller, to that seen in N-body simulations. It is large for low mass haloes $M \ll M_\star$, and fades as we go to high masses $M > M_\star$ as a result of a genuine statistical effect, namely, the decrease in average asymmetry and stochasticity with increasing halo mass. Haloes that formed at high redshift are found to be more clustered than those that assembled recently. This is precisely the behaviour reported by Gao, Springel & White (2005). However, haloes in denser regions are predicted to assemble later. This result is inconsistent with the trend measured in overdense environments $\delta \gtrsim 0$. It calls into question the role of the ellipsoidal collapse in shaping the halo mass function. Nevertheless, several lines of recent evidence indicate that, in relatively underdense regions, the average formation redshift increases with decreasing environment density (e.g. Harker *et al.* 2006), while haloes may be more strongly clustered than the mean (Abbas & Sheth 2007). Our model predicts and effect in the right sense. This suggests that the ellipsoidal collapse model may be applicable in underdense regions, where tidal interactions are weak or absent. Conditional halo mass functions $n(M|\delta)$ could provide another testable prediction since, in the moving barrier interpretation adopted here, it is expected that $n(M|\delta)$ in underdense regions should be (slightly) biased towards high mass haloes as compared to the prediction of Sheth & Tormen (2002).

Recently, Sandvik *et al.* (2007) have discussed a multi-dimensional extension of the EPS formalism that takes into account ellipsoidal collapse (Chiueh & Lee 2001). They find a very weak correlation between halo assembly history and environment, presumably because their implementation includes only the statistical aspect of environmental effects. In our scenario, the dynamical interaction between the external mass distribution and the collapsing halo plays a crucial role in the environmental dependence of halo properties. The statistical correlations contribute mostly to increase the strength of the effect with decreasing halo mass.

A serious shortcoming of our model is the neglect of anisotropies beyond the quadrupole term in the external density field. Furthermore, apart from a global rotation, it ignores the non-radial degrees of freedom in the collapsing protohalo. It would be of great interest to ascertain whether non-radial motions created by a clumpy, growing large scale mass distribution can induce an effect similar to that seen in simulations. *A priori*, tidal heating should be more efficient in high density environments. It may plausibly reverse the trend found in this paper, namely, increase the critical collapse density in large scale overdensities. If this happens to be true, a moving barrier approach would naturally predict haloes in dense regions to assemble relatively early and to be more strongly clustered than the mean. Alternatively, Wang *et al.* (2007) have suggested that tidal heating causes haloes to appear less massive than expected from their initial

density field. This may also provide an explanation for the relatively large/low bias of old/young haloes. Clearly, large N-body simulations are needed to understand the complex relations reported by, e.g. Harker *et al.* (2006), Wechsler *et al.* (2006), Gao & White (2007). This caveat notwithstanding, analytic models can provide an elegant route to capturing the essential features of the environmental dependence.

In standard galaxy formation models, the correlation between the haloes and their large scale environment introduces a correlation between the properties of galaxies and the regions they occupy (e.g. Abbas & Sheth 2005, 2006; Berlind *et al.* 2005). The observational results of Skibba *et al.* (2006), Blanton *et al.* (2006) and Tinker *et al.* (2007) support this prediction and leave little room for a galaxy assembly bias (see, however, Croton *et al.* 2007). Nevertheless, the influence of the environmental dependence of halo properties on the galaxy population remains unclear. It would be valuable to assess whether environmental effects produced by the anisotropic collapse of haloes can leave a detectable signature in the properties of field galaxies.

ACKNOWLEDGEMENTS

I wish to thank Avishai Dekel, André Henriques, Yehuda Hoffman, Eyal Neistein and Adi Nusser for helpful discussions; Havard Sandvik and Geraint Harker for correspondence; and Noam Libeskind for his comments on a early version of this manuscript. This work has been supported by the German-Israel Einstein Centre and a Golda Meir Fellowship at the Hebrew University.

REFERENCES

Abbas U., Sheth R.K., 2005, MNRAS, 364, 1327
Abbas U., Sheth R.K., 2006, MNRAS, 372, 1749
Abbas U., Sheth R.K., 2007, MNRAS, 378, 641
Adler R.J., 1981, The Geometry of Random Fields (Chichester:Wiley)
Amosov G., Schücker P., 2004, A&A, 421 425
Arnold V.I., Shandarin S.F., Zeldovich Y.B., 1982, Geophys. Astrophys.. Fluid Dyn., 20, 111
Audit A., Alimi J-M., 1996, A&A, 315, 11
Audit E., Teyssier R., Alimi J-M., 1997, A&A, 325, 439
Balantekin A.B., 2000, Phys. Rev. D, 62, 085017
Bardeen J.M., Bond J.R., Kaiser N., Szalay A.S., 1986, ApJ, 304, 15
Barnes J., Efstathiou G., 1987, ApJ, 319, 575
Barrow J., Silk J., 1981, ApJ, 250, 432
Berlind A.A., Blanton M.R., Hogg D.W., Weinberg D.H., Davé R., Eisenstein D.J., Katz N., 2005, ApJ, 629, 625
Berntsen J., Espelid T.O., Genz A., 1991, ACM Transactions on Mathematical Software, 17, 452
Bertschinger E., Gelb J.M., 1991, Comp. Phys., 5, 164
Bertschinger E., Jain B., 1994, ApJ, 431, 486
Bett P., Eke V., Frenk C.S., Jenkins A., Helly J., Navarro J., 2007, MNRAS, 376, 215
Binney J., Tremaine S., 1987, Galactic Dynamics (Princeton: Princeton University Press)
Bond J.R., Cole S., Efstathiou G., Kaiser N., 1991, ApJ, 379, 440
Bond J.R., Myers S., 1996, ApJS, 103, 1
Bond J.R., Kofman L., Pogosyan D., 1996, Nature, 380, 603
Bower R.G., 1991, 248, 332
Bullock J.S., Dekel A., Kolatt T.S., Kravtsov A.V., Klypin A.A., Porciani C., Primack J.R., 2001, ApJ, 555, 240
Catelan P., Theuns T., 1996, MNRAS, 282, 436
Catelan P., Lucchin F., Matarrese S., Porciani C., 1998, MNRAS, 297, 692
Catelan P., Porciani C., 2001, MNRAS, 323, 713
Cen R., Ostriker J.P., 1993, ApJ, 417, 415
Chandrasekhar S., 1969, Ellipsoidal Figures of Equilibrium (New York: Dover)
Chiueh T., Lee J., 2001, ApJ, 555, 83
Colombi S., Pogosyan D., Souradeep T., 2000, Phys. Rev. Lett., 85, 5515
Croton D.J., Gao L., White S.D.M., 2007, MNRAS, 374, 1303
Diemand J., Kuhlen M., Madau P., 2007, preprint, astro-ph/0703337
Del Popolo A., Gambera M., 1998, A&A, 337, 96
Del Popolo A., Ercan E.N., Xia Z., 2001, AJ, 122, 487
Doroshkevich A.G., 1970, Astrofizika, 3, 175
Doroshkevich A.G., Shandarin S.F., 1978, Soviet. Astr., 22, 653
Dubinski J., 1992, ApJ, 401, 441
Eisenstein D.J., Loeb A., 1995, ApJ, 439, 520
Eisenstein D.J., Hu W., 1999, ApJ, 511, 5
Eke V.R., Cole S., Frenk C.S., 1996, MNRAS, 282, 263
Fujimoto M., 1968, ApJ, 152, 523
Furlanetto S.R., Kamionkowski M., 2006, MNRAS, 366, 529
Gao L., Springel V., White S.D.M., 2005, 363, L66
Gao L., White S.D.M., 2007, MNRAS, 377, L5
Giocoli C., Moreno J., Sheth R.K., Tormen G., 2007, MNRAS 376, 977
Gleser L., Nusser A., Ciardi B., Desjacques V., 2006, MNRAS, 370, 1329
Gradshteyn I.S., Ryzbik I.M., 2000, Table of Integrals, Series and Products, 6th Edition (New York: Academic)
Gunn J.E., Gott J.R. III, 1972, ApJ, 176, 1
Hahn O., Porciani C., Carollo C.C., Dekel A., 2007, MNRAS, 375, 489
Hanami H., 2001, MNRAS, 327, 721
Harish Chandra, 1958, Am. J. Phys., 80, 241
Harker G., Cole S., Helly J., Frenk C., Jenkins A., 2006, MNRAS, 367, 1039
Hoffman Y., 1986, ApJ, 308, 493
Hoffman Y., 1988, ApJ, 329, 8
Hoffman Y., Ribak E., 1991, ApJ, 380, L5
Hua L.K., 1963, Harmonic Analysis of Functions of Several Complex Variables in the Classical Domains (Providence: American Mathematical Society)
Hui L., Bertschinger E., 1996, ApJ, 471, 1
Icke V., 1973, A&A, 27, 1
Itzykson C., Zuber J.B., 1980, J. Math. Phys., 21, 411
Jing Y.P., Suto Y., 2002, ApJ, 574, 538
Jing Y.P., Suto Y., Mo H.J., 2007, ApJ, 657, 664
Kaiser N., 1984, ApJ, 284, 9
Kauffmann G., White S.D.M., 1993, MNRAS, 261, 921
Kitayama T., Suto Y., 1996, MNRAS, 280, 638
Lacey C., Cole S., 1993, MNRAS, 262, 627
Lee J., Shandarin S., 1998, ApJ, 500, 14
Lee J., Pen U.-L., 2001, ApJ, 555, 106
Lemson G., 1993, MNRAS, 263, 913
Lemson G., Kauffmann G., 1999, MNRAS, 302, 111
Lin C.C., Mestel L., Shu F.H., 1965, ApJ, 142, 1431
Lin W.P., Jing Y.P., Lin L., 2003, MNRAS, 344, 1327L
Lokas E.L., Juskiewicz R., Bouchet F.R., Hivon E., 1996, ApJ, 467, 1
Lokas E.L., Hoffman Y., in Proceedings of the Third International Workshop on the Identification of Dark Matter, ed. N.J.C. Spooner and V. Kudryavtsev (Singapore: World Scientific)
Lynden-Bell D., 1964, ApJ, 139, 1195
Mo H.J., White S.D.M., 1996, MNRAS, 282, 347

Mo H.J., Jing Y., White S.D.M., 1997, MNRAS, 284, 189
Monaco P., 1995, ApJ, 447, 23
Monaco P., 1997a, MNRAS, 287, 753
Monaco P., 1997b, MNRAS, 290, 439
Nagashima M., 2001, ApJ, 562, 7
Navarro J.F., Frenk C.S., White S.D.M., 1997, ApJ, 490, 493
Neistein E., Van den Bosch F.C., Dekel A., 2006, MNRAS, 372, 933
Neistein E., Dekel A., 2007, in preparation
Novikov D., Colombi S., Doré O., 2006, MNRAS, 366, 1201
Nusser A., Colberg J., 1998, MNRAS, 294, 457
Park C., 1990, MNRAS, 242, 59
Peacock J.A., Heavens A.F., 1985, MNRAS, 217, 805
Peacock J.A., Heavens A.F., 1990, MNRAS, 243, 133
Peebles P.J.E., 1969, ApJ, 155, 393
Peebles P.J.E., Groth E.J., 1976, A&A, 53, 131
Peebles P.J.E., 1980, The Large Scale Structure of the Universe (Princeton: Princeton University Press)
Peebles P.J.E., 1990, ApJ, 365, 27
Percival W.J., Scott D., Peacock J.A., Dunlop J.S., 2003, MNRAS, 338, L31
Pogosyan D., Bond J.R., Kofman L., Wadsley J., 1998, in Proceedings of the XIV IAP Colloquium, Wide Field Surveys in Cosmology, ed. Y. Mellier and S. Colombi (Paris: Editions Frontieres)
Porciani C., Dekel A., Hoffman Y., 2002a, MNRAS, 332, 325
Porciani C., Dekel A., Hoffman Y., 2002b, MNRAS, 332, 339
Press W.H., Schechter P., 1974, ApJ, 187, 425
Quinn T., Binney J., 1992, MNRAS, 255, 729
Ryden B.S., Gunn J.E., 1987, ApJ, 318, 15
Ryden B.S., 1988, ApJ, 329, 589
Sakurai J.J., 1985, Modern Quantum Mechanics (New York: Addison-Wesley)
Sandvik H.B., Möller O., Lee J., White S.D.M., 2007, MNRAS 377, 234
Schücker P., Böhringer H., Arzner K., Reiprich T.K., 2001, A&A, 370, 715
Sahni V., Sathyaprakash B.S., Shandarin S.F., 1998, ApJ, 495, L5
Shandarin S.F., Klypin A.A., 1984, Soviet Astron., 28, 491
Shandarin S.F., Melott A.L., Mcdavitt K., Pauls J.L., Tinker J., 1995, Phys. Rev. Lett., 75, 7
Shen J., Abel T., Mo H., Sheth R.K., 2006, ApJ, 645, 783
Sheth R.K., 1998, MNRAS, 300, 1057
Sheth R.K., Lemson G., 1999a, MNRAS, 304, 767
Sheth R.K., Lemson G., 1999b, MNRAS, 305, 946
Sheth R.K., Tormen G., 1999c, MNRAS, 308, 119
Sheth R.K., Mo H.J., Tormen G., 2001, MNRAS, 323, 1
Sheth R.K., Tormen G., 2002, MNRAS, 329, 61
Sheth R.K., Tormen G., 2004, MNRAS, 350, 1385
Skibba R., Sheth R.K., Connolly A.J., Scranton R., 2006, MNRAS, 369, 68
Sousbie T., Pichon C., Colombi S., Novikov D., Pogosyan D., preprint, astro-ph/0707.3123
Springel V. *et al.* , 2005, Nat, 435, 639
Steinmetz M., Bartelmann M., 1995, MNRAS, 272, 570
Szalay A.S., Silk J., 1983, ApJ, 308, 499
Tinker J.L., Conroy C., Norberg P., Patiri S.G., Weinberg D.H., Warren M.S., 2007, preprint, astro-ph/0707.3445
Van de Weygaert R., Bertschinger E., 1996, MNRAS, 281, 84
Van Den Bosch F.C, 2002, MNRAS, 331, 98
Villumsen J.V., Davis M., 1986, ApJ, 308, 499
Wang H.Y., Mo H.J., Jing Y.P., 2007, MNRAS, 375, 633
Wechsler R.H., Zenter A.R., Bullock J.S., Kravtsov A.V., Allgood B., 2006, ApJ, 652, 71
Wei G., Eichinger B.E., 1989, Macromolecules, 22 1989
Wei G., Eichinger B.E., 1990, J. Math. Phys., 31, 11
Wetzel A.R., Cohn J.D., White M., Holz D.E., Warren M.S., 2007, ApJ, 656, 139
Weyl H., 1948, The Classical Groups (Princeton: Princeton University Press)
White S.D.M., Silk J., 1979, ApJ, 231, 1
White S.D.M., 1984, ApJ, 286, 38
White S.D.M., 1996, in Cosmology and Large scale Structure, Proceedings of the 60th Les Houches School, ASP. Conf. Ser. 176, 349 (Amsterdam: Elsevier)
Zeldovich Y.B., 1970, A&A, 5, 84
Zentner A.R., Berlind A.A., Bullock J.S., Kravstov A.V., Wechsler R.H., 2005, ApJ, 624, 505
Zentner A.R., 2007, IJMPD, 16, 763
Zhu G., Zheng Z., Lin W.P., Jing Y.P., Kang X., Gao L., 2006, ApJ, 639, L5

APPENDIX A: TWO-POINT CORRELATIONS OF THE SHEAR TENSOR

We consider the two-point correlation functions of an arbitrary symmetric tensor field $\mathrm{T}_{ij}(\boldsymbol{x})$. Statistical isotropy and symmetry imply that, in position space, these correlations must be of the form

$$\begin{aligned}\langle \mathrm{T}_{ij}(\boldsymbol{x})\mathrm{T}_{lm}(\boldsymbol{x}+\boldsymbol{r})\rangle &= \Psi_1(r)\,\hat{r}_i\hat{r}_j\hat{r}_l\hat{r}_m \\ &+ \Psi_2(r)\,(\hat{r}_i\hat{r}_l\delta_{jm}+\hat{r}_i\hat{r}_m\delta_{jl}+\hat{r}_j\hat{r}_l\delta_{im}+\hat{r}_j\hat{r}_m\delta_{il}) \\ &+ \Psi_3(r)\,(\hat{r}_i\hat{r}_j\delta_{lm}+\hat{r}_l\hat{r}_m\delta_{ij})+\Psi_4(r)\,\delta_{ij}\delta_{lm} \\ &+ \Psi_5(r)\,(\delta_{il}\delta_{jm}+\delta_{im}\delta_{jl})\ , \end{aligned} \tag{A1}$$

where $\hat{r}_i = r_i/|\boldsymbol{r}|$ and the functions $\Psi_i(r)$ depend on $r = |\boldsymbol{r}|$ only. This is the most general ansatz for a symmetric, isotropic correlation tensor. In the case of a scalar (spin-0) tensor such as the shear ξ_{ij} defined in eq. (1), $\Psi_2 = \Psi_3$ and $\Psi_4 = \Psi_5$. Explicit expression for the functions $\Psi_i(r)$ can be obtained from the Fourier transform of $\langle \xi_{ij}(\boldsymbol{x})\xi_{lm}(\boldsymbol{x}+\boldsymbol{r})\rangle$,

$$\langle \xi_{ij}(\boldsymbol{k})\xi_{lm}(\boldsymbol{k})\rangle = P_\delta(k)\,\hat{k}_i\hat{k}_j\hat{k}_l\hat{k}_m\ , \tag{A2}$$

where $\hat{k}_i = k_i/k$ and $P_\delta(k)$ is the power spectrum of the density field $\delta(\boldsymbol{x})$. The following integrals are useful to the calculation of $\Psi_i(r)$,

$$\begin{aligned}\frac{1}{2}\int_{-1}^{+1}\mathrm{d}\mu\,\mu^2\,e^{ikr\mu} &= \frac{1}{3}j_0(kr)-\frac{2}{3}j_2(kr) \\ \frac{1}{2}\int_{-1}^{+1}\mathrm{d}\mu\,\mu^4\,e^{ikr\mu} &= \frac{1}{5}j_0(kr)-\frac{4}{7}j_2(kr)+\frac{8}{35}j_4(kr)\ , \end{aligned} \tag{A3}$$

where $j_\ell(x)$ are spherical Bessel functions of the first kind. With these informations, the functions Ψ_i may be conveniently expressed as

$$\begin{aligned}\Psi_1(r) &= \int_0^\infty \mathrm{d}\ln k\,\Delta^2_\delta(k)\,j_4(kr) \\ \Psi_3(r) &= \int_0^\infty \mathrm{d}\ln k\,\Delta^2_\delta(k)\,\left[-\frac{1}{7}j_2(kr)-\frac{1}{7}j_4(kr)\right] \\ \Psi_5(r) &= \int_0^\infty \mathrm{d}\ln k\,\Delta^2_\delta(k)\,\left[\frac{1}{15}j_0(kr)+\frac{2}{21}j_2(kr)+\frac{1}{35}j_4(kr)\right] \end{aligned} \tag{A4}$$

In the limit $r \to 0$, both Ψ_1 and Ψ_3 vanish, but $\Psi_5 = \xi_{01}/15$ (Figure A1). Notice that the functions Ψ_i can also be cast into the form given in, e.g., Lee & Pen (2001) and Catelan & Porciani (2001), which involves $J_n \equiv nr^{-n}\int_0^r \mathrm{d}s\,\xi(s)s^{n-1}$ (this is best seen by integrating J_n by part).

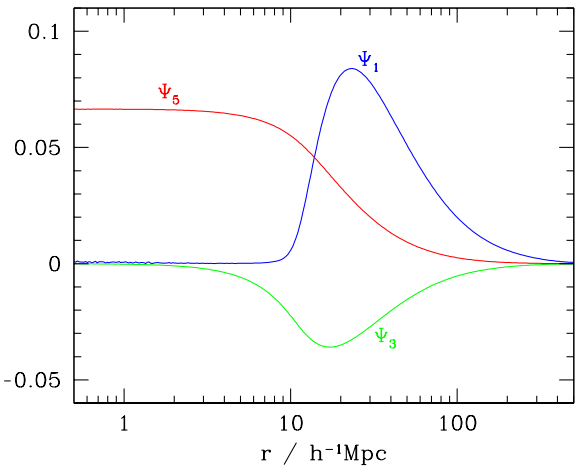

Figure A1. The correlation functions $\Psi_1(r)$, $\Psi_3(r)$ and $\Psi_5(r)$ as a function of comoving separation r for the ΛCDM cosmology considered in this paper. They are normalised by ξ_{01} (eq. 9). The shear tensor at position $\boldsymbol{x}$ and $\boldsymbol{x}+\boldsymbol{r}$ is smoothed on scale $R_0 = 10$ and $R_1 = 2\ h^{-1}$Mpc, respectively. Note that Ψ_1 is strongly suppressed on scale $r \lesssim R_0$.

APPENDIX B: AN INTEGRAL OVER THE SO(3) MANIFOLD

In this Appendix, we present the calculation of the integral eq. (18) over the special orthogonal group SO(3), where α and λ are real symmetric matrices.

Let $\mathrm{R} \equiv \mathrm{R}_{\hat{\boldsymbol{n}}}(\varphi)$ be the rotation by an angle φ about the axis $\hat{\boldsymbol{n}}$. Since the Haar measure dR is invariant under both left and right transformations, we can redefine R so as to diagonalise λ and α. We will therefore assume that the matrices λ and α are diagonal, $\lambda = \mathrm{diag}(\lambda_i)$ and $\alpha = \mathrm{diag}(\alpha_i)$. It is worth noting that α and λ are not orthogonal matrices, but belong to the (real) linear group GL(3,R). Consider now the rotation of π around the first axis, $\sigma_1 = \mathrm{diag}(1,-1,-1)$, and its distinct permutations $\sigma_2 = \mathrm{diag}(-1,1,-1)$ and $\sigma_3 = \mathrm{diag}(-1,-1,1)$. Since the compositions $\sigma_i\mathrm{R}$ characterise equivalent principal axis frames, the integral (18) should in principle be performed over the quotient space $\mathrm{SO}(3)/\{\sigma_1,\sigma_2,\sigma_3\}$. However, the σ_is are diagonal and we find

$$\mathrm{tr}\left[(\sigma_i\mathrm{R})\,\lambda\,(\sigma_i\mathrm{R})^\top\alpha\right] = \mathrm{tr}\left(\mathrm{R}\lambda\mathrm{R}^\top\alpha\right)\ . \tag{B1}$$

Therefore, one can also perform the integration over the whole orthogonal group SO(3) and multiply the final result by 1/4.

Integrals of the form

$$F(\alpha,\lambda) = \int_{\mathrm{G}} \mathrm{d}\Omega\, e^{\beta\mathrm{tr}\left(\Omega\lambda\Omega^{-1}\alpha\right)} \tag{B2}$$

where G ($\Omega \in$G) is a compact Lie group and α, λ belong to the linear group GL, appear in Quantum Field Theory, chemistry as well as in harmonic analysis (e.g. Hua 1963; Itzykson & Zuber 1980; Wei & Eichinger 1989). When G is the unitary group U(N), group theoretical techniques such as character expansion can be used to obtain a closed form determinantal evaluation of (B2) (e.g. Harish Chandra 1958; Balantekin 2000). Unfortunately, these methods cannot be easily applied when G is the orthogonal group SO(N), essentially because the representations of SO(N) and GL(N,R) are very different. Instead, one generally relies on a specific parametrisation of the rotation matrices and express the result in terms of a series of orthogonal functions.

Here we follow the approach outlined in Wei & Eichinger (1990) and parametrise the special rotation matrices R in terms of the Euler angles $0 \le \varphi, \psi \le 2\pi$, $0 \le \vartheta \le \pi$,

$$\mathrm{R} = \begin{pmatrix} c_\psi c_\varphi - c_\vartheta s_\varphi s_\psi & c_\psi s_\varphi + c_\vartheta c_\varphi s_\psi & s_\psi s_\vartheta \\ -s_\psi c_\varphi - c_\vartheta s_\varphi c_\psi & -s_\psi s_\varphi + c_\vartheta c_\varphi c_\psi & c_\psi s_\vartheta \\ s_\vartheta s_\varphi & -s_\vartheta c_\varphi & c_\vartheta \end{pmatrix}, \tag{B3}$$

where $c_\psi = \cos\psi$, $s_\varphi = \sin\varphi$ etc. Notice that this representation becomes singular when $\vartheta = 0$ or π (such singularities are expected owing to the topology of SO(3)). The original integral (18) over the SO(3) manifold can be written as a triple integral with the (normalised) invariant measure $\mathrm{dR} = 1/(8\pi^2)\sin\vartheta\,\mathrm{d}\varphi\mathrm{d}\vartheta\mathrm{d}\psi$,

$$F(\alpha,\lambda) = \frac{1}{8\pi^2}\int_0^{2\pi}\mathrm{d}\varphi\int_0^{\pi}\mathrm{d}\vartheta\,\sin\vartheta\int_0^{2\pi}\mathrm{d}\psi\, e^{\beta\mathrm{tr}\left(\mathrm{R}\lambda\mathrm{R}^\top\alpha\right)}\ . \tag{B4}$$

Since the integrand is invariant under the transformations $(\alpha,\lambda) \to \left(k\,\alpha, \frac{1}{k}\,\lambda\right)$ and $(\alpha,\lambda) \to \left(\alpha + k\,\mathrm{I}, \lambda - \frac{k\,\mathrm{tr}\lambda}{k+\mathrm{tr}\alpha}\,\mathrm{I}\right)$, where k is a real number and I is the 3×3 identity matrix, $F(\alpha,\lambda)$ can be expressed as a function of four variables instead of the original six matrix eigenvalues. This can also seen by rewriting the trace as (Wei & Eichinger 1990)

$$\mathrm{tr}\left(\mathrm{R}\lambda\mathrm{R}^\top\alpha\right) = \frac{1}{3}\left(\mathrm{tr}\alpha\,\mathrm{tr}\lambda - \mathrm{tr}\tilde{\alpha}\,\mathrm{tr}\tilde{\lambda}\right) + \mathrm{tr}\left(\mathrm{R}\tilde{\lambda}\mathrm{R}^\top\tilde{\alpha}\right)\ . \tag{B5}$$

where, for instance, $\tilde{\alpha} = \mathrm{diag}\,(\alpha_{13},\alpha_{23},0)$, $\tilde{\lambda} = \mathrm{diag}\,(\lambda_{13},\lambda_{23},0)$, $\alpha_{ij} = \alpha_i - \alpha_j$ and $\lambda_{ij} = \lambda_i - \lambda_j$. We enforce the ordering $\alpha_1 \ge \alpha_2 \ge \alpha_3$ and $\lambda_1 \ge \lambda_2 \ge \lambda_3$, so that $\alpha_{13}, \alpha_{23} \ge 0$ and $\lambda_{13}, \lambda_{23} \ge 0$. The integral depends now on four distinct combinations of the αs and λs: $\epsilon_+ = (1/3)\,\mathrm{tr}\alpha\,\mathrm{tr}\lambda$, $\epsilon_- = (1/3)\,\mathrm{tr}\tilde{\alpha}\,\mathrm{tr}\tilde{\lambda}$, $\epsilon_\alpha = \alpha_{12}/\mathrm{tr}\tilde{\alpha}$, $\epsilon_\lambda = \lambda_{12}/\mathrm{tr}\tilde{\lambda}$. With this parametrisation, $-\infty \le \epsilon_+ \le \infty$, $\epsilon_- \ge 0$ and $0 \le \epsilon_\alpha, \epsilon_\lambda \le 1$.

We can expand the trace in terms of the Wigner D-functions $\mathcal{D}^l_{m_1,m_2}$, l being the index of the representation (see, e.g., Sakurai 1985). These 3D harmonics generate irreducible representations of the three-dimensional rotation group and, therefore, form a complete orthogonal set of functions defined on SO(3) itself. Unsurprisingly, only the quadrupole ($l = 2$) rotation matrices appear in the trace decomposition,

$$\begin{aligned}\mathrm{tr}\left(\mathrm{R}\tilde{\lambda}\mathrm{R}^\top\tilde{\alpha}\right) = \frac{\epsilon_-}{2}\Bigg[&\frac{2}{3} + \mathcal{D}^2_{0,0} \\ &+ \sqrt{\frac{3}{2}}\epsilon_\alpha\left(\mathcal{D}^2_{0,-2} + \mathcal{D}^2_{0,2}\right) + \sqrt{\frac{3}{2}}\epsilon_\lambda\left(\mathcal{D}^2_{-2,0} + \mathcal{D}^2_{2,0}\right) \\ &+ \frac{3}{2}\epsilon_\alpha\epsilon_\lambda\left(\mathcal{D}^2_{-2,-2} + \mathcal{D}^2_{2,2} + \mathcal{D}^2_{-2,2} + \mathcal{D}^2_{2,-2}\right)\Bigg]\ .\end{aligned} \tag{B6}$$

The explicit form of these $l = 2$ harmonics is given in Table B1. Note that $\mathrm{tr}(\mathrm{R}\tilde{\lambda}\mathrm{R}^\top\tilde{\alpha})$ depends on the three "shape" parameters ϵ_-, ϵ_α and ϵ_λ solely, because points on SO(3) truly have only three degrees of freedom. The integral over the variable ψ can be performed using the following identity (see §3.937 of Gradshteyn & Ryzbik 2000),

$$\frac{1}{2\pi}\int_0^{2\pi}\mathrm{d}\psi\, e^{\beta[x\cos(2\psi)+y\sin(2\psi)]} = I_0\left(\sqrt{x^2+y^2}\right)\ , \tag{B7}$$

Table B1. Quadrupole Wigner D-functions $\mathcal{D}^2_{m_1,m_2}(\varphi,\vartheta,\psi)$ (Harmonics with $m_1, m_2 = \pm 1$ are not shown).

	$m_2=-2$	$m_2=0$	$m_2=2$
$m_1=-2$	$\frac{1}{4}(1+\cos\vartheta)^2\, e^{-2i\varphi-2i\psi}$	$\sqrt{\frac{3}{8}}\sin^2\vartheta\, e^{-2i\varphi}$	$\frac{1}{4}(1-\cos\vartheta)^2\, e^{-2i\varphi+2i\psi}$
$m_1=0$	$\sqrt{\frac{3}{8}}\sin^2\vartheta\, e^{-2i\psi}$	$\frac{1}{2}\left(3\cos^2\vartheta-1\right)$	$\sqrt{\frac{3}{8}}\sin^2\vartheta\, e^{2i\psi}$
$m_1=2$	$\frac{1}{4}(1-\cos\vartheta)^2\, e^{2i\varphi-2i\psi}$	$\sqrt{\frac{3}{8}}\sin^2\vartheta\, e^{2i\psi}$	$\frac{1}{4}(1+\cos\vartheta)^2\, e^{2i\varphi+2i\psi}$

where I_0 is a modified Bessel function of the first kind. The result can be written

$$F(\alpha,\lambda) = e^{\beta\epsilon_+}\, W\left(\beta\epsilon_-,\epsilon_\alpha,\epsilon_\lambda\right)\ . \tag{B8}$$

where the function $W\left(\beta\epsilon_-,\epsilon_\alpha,\epsilon_\lambda\right)$ is a double integral which can be arranged such that

$$\begin{aligned} &W\left(\beta\epsilon_-,\epsilon_\alpha,\epsilon_\lambda\right) \\ &\quad = \ e^{-\beta\epsilon_-}\ \left\{\frac{1}{2\pi}\int_0^1 \mathrm{d}r \int_0^{2\pi} \mathrm{d}\varphi\ \exp\left[\frac{3\beta\,\epsilon_-}{4}\, g(r,\varphi,\epsilon_\alpha)\right]\right. \\ &\qquad \left.\times I_0\left[\frac{3\beta\,\epsilon_-\epsilon_\lambda}{4}\sqrt{h(r,\varphi,\epsilon_\alpha)}\right]\right\}\ , \end{aligned} \tag{B9}$$

where $r = -\cos\vartheta$. The functions $g(r,\varphi,\epsilon_\alpha)$ and $h(r,\varphi,\epsilon_\alpha)$ are defined as

$$\begin{aligned} g(r,\varphi,\epsilon_\alpha) \ &= \ 1 + r^2 + \epsilon_\alpha\left(1-r^2\right)\cos(2\varphi) \\ h(r,\varphi,\epsilon_\alpha) \ &= \ g^2 - 4\left(1-\epsilon_\alpha^2\right) r^2\ . \end{aligned} \tag{B10}$$

They are periodic of period π in the argument φ. Furthermore, on the domain defined by $0 \le r \le 1$ and $0 \le \varphi \le 2\pi$, the function g is bounded by $1-\epsilon_\alpha \le g(r,\varphi,\epsilon_\alpha) \le 1+\epsilon_\alpha$. Consequently, the double integral that appears in eq. (B9) is always larger than or equal to 1. The equality holds only when α and/or λ is proportional to the identity matrix.

Expanding the integrand of (B9) about $\beta\epsilon_- = 0$ gives, upon integration, the following series

$$\begin{aligned} &W\left(\beta\epsilon_-,\epsilon_\alpha,\epsilon_\lambda\right) \\ &\quad \approx e^{-\beta\epsilon_-}\left[1 + \frac{\beta^2\epsilon_-^2}{40}p_1(\epsilon_\alpha)p_1(\epsilon_\lambda) + \frac{\beta^3\epsilon_-^3}{840}p_2(\epsilon_\alpha)p_2(\epsilon_\lambda)\right. \\ &\quad \left. + \frac{\beta^4\epsilon_-^4}{4480}p_1^2(\epsilon_\alpha)p_1^2(\epsilon_\lambda) + \frac{\beta^5\epsilon_-^5}{73920}p_1(\epsilon_\alpha)p_2(\epsilon_\alpha)p_1(\epsilon_\lambda)p_2(\epsilon_\lambda)\right] \end{aligned} \tag{B11}$$

where $p_1(x) = (3x^2+1)$ and $p_2(x) = (9x^2-1)$. We have found that this truncated, fifth-order expansion is accurate to within 2 per cent in the range $0 \le \beta\epsilon_- \lesssim 1.5$ and can be used efficiently in the computation of the group integral (18). Conditional probability distributions for the relative orientation can be derived in a straightforward way from the preceding results.

Noteworthy is the special case G=SO(2), in which the integral (B2) can be written in closed form,

$$F(\alpha,\lambda) = e^{\beta\epsilon_+} I_0\left(\frac{1}{2}\alpha_{12}\lambda_{12}\right)\ , \tag{B12}$$

where the parameter ϵ_+ is now $\epsilon_+ = (1/2)\,\mathrm{tr}\alpha\,\mathrm{tr}\lambda$.

APPENDIX C: POTENTIAL OF A HOMOGENEOUS ELLIPSOID

For a homogeneous ellipsoid defined such that $\rho(\boldsymbol{r}) = \delta\rho$ if $\boldsymbol{r}^\top\left(\mathrm{A}\mathrm{A}^\top\right)^{-1})\,\boldsymbol{r} \le 1$, and zero otherwise, the potential at any exterior point $\boldsymbol{r} = (r_1, r_2, r_3)$ is (Kellog 1929; Chandrasekhar 1969)

$$\Phi_e(\boldsymbol{r}) = \pi G\delta\rho\ \left[C(\rho) - \sum_i b_i(\rho)\, r_i^2\right]\ , \tag{C1}$$

while the potential inside and on the boundary of the ellipsoid is

$$\Phi_i(\boldsymbol{r}) = \pi G\delta\rho\ \left[C(0) - \sum_i b_i(0)\, r_i^2\right]\ . \tag{C2}$$

$AA^\top$ is a positive definite matrix whose eigenvalues are the square of the principal axis lengths $A_1 \ge A_2 \ge A_3 > 0$. The variable ρ is defined as the algebraically largest root of the following cubic equation,

$$\frac{x^2}{A_1^2+\rho} + \frac{y^2}{A_2^2+\rho} + \frac{z^2}{A_3^2+\rho} = 1\ . \tag{C3}$$

The functions $C(\rho)$ and $b_i(\rho)$ are given by

$$\begin{aligned} C(\rho) \ &= \ A_1A_2A_3\int_\rho^\infty \frac{\mathrm{d}u}{\Delta(u)} \\ b_i(\rho) \ &= \ A_1A_2A_3\int_\rho^\infty \frac{\mathrm{d}u}{\left(A_i^2+u\right)\Delta(u)}\ , \end{aligned} \tag{C4}$$

where $\Delta(u) \ = \ \Pi_{k=1}^3\left(A_k^2+u\right)^{1/2}$. These functions can be expressed in terms of the Legendre's incomplete elliptic integrals of first and second kind (Binney & Tremaine 1987). The gravitational potential energy of this self-gravitating ellipsoid is

$$E_{\rm pot} = -\frac{3}{10}\, GM^2\int_0^\infty \frac{\mathrm{d}u}{\Delta(u)} \tag{C5}$$

and is proportional to the potential at $\boldsymbol{x} = 0$, $C(0)$. Notice also that Poisson's equation implies $\sum_i b_i(0) = 2$.